HUBBLE SPACE TELESCOPE OBSERVATIONS OF 10 TWO-IMAGE GRAVITATIONAL LENSES[1]

J. LEHÁR,[2] E. E. FALCO,[2] C. S. KOCHANEK,[2] B. A. MCLEOD,[2] J. A. MUÑOZ,[2] C. D. IMPEY,[3] H.-W. RIX,[4] C. R. KEETON,[3] AND C. Y. PENG[3]

ABSTRACT

We report on a program to obtain *Hubble Space Telescope* (*HST*) observations of galaxy-mass gravitational lens systems at optical and infrared wavelengths. Here we discuss the properties of 10 two-image gravitational lens systems (Q0142−100 = UM 673, B0218+357, SBS 0909+532, BRI 0952−0115, LBQS 1009−0252, Q1017−207 = J03.13, B1030+074, HE 1104−1805, Q1208+1011, and PKS 1830−211). We grouped these 10 systems because they have limited lens model constraints and often show poor contrast between the images and the lens galaxy. Of the 10 lens galaxies, seven are probably early-type galaxies, two are probably late-type galaxies (B0218+357 and PKS 1830−211), and one was not detected (Q1208+1011). We detect the host galaxies of the $z_s = 4.50$ lensed quasar in BRI 0952−0115, the $z_s = 2.32$ lensed quasar in HE 1104−1805, and the unlensed $z = 1.63$ quasar near LBQS 1009−0252. We fit a set of four standard lens models to each lens that had sufficient constraints to compare isothermal dark matter and constant mass-to-light lens models, and to explore the effects of local tidal shears.

Subject headings: galaxies: fundamental parameters — gravitational lensing

1. INTRODUCTION

Gravitational lenses have become extraordinarily useful tools for cosmology, galactic structure, and galactic evolution (for example, see Schneider, Ehlers, & Falco 1992; Blandford & Narayan 1992). With approximately 60 known lenses produced by galaxies (see Keeton & Kochanek 1996 for a recent but now quite incomplete summary[5]), small number statistics are rapidly becoming a problem of the past. Preliminary studies have shown that lens systems have mass-to-light ratios (M/L) that are 50%–100% higher than found in constant M/L stellar dynamical models locally, consistent with the expectation for early-type galaxies embedded in massive dark halos (Kochanek 1996; Keeton, Kochanek, & Falco 1998, hereafter KKF; Jackson et al. 1998). The mass and light distributions are generally aligned but have different quadrupole moments (KKF). Where simple ellipsoidal models suggest a mass distribution that is misaligned with the light, the cause seems to be external tidal perturbations from nearby objects. In fact, Keeton, Kochanek, & Seljak (1997) found that all four-image lenses required two axes for the angular structure of the potential to obtain a good fit, where the two axes are presumably the major axis of the primary lens and the axis of the local tidal gravity field. The lens galaxies generally have the colors and shapes of early-type galaxies rather than spiral galaxies (KKF), consistent with theoretical expectations for their relative lensing cross sections (e.g., Turner, Ostriker, & Gott 1984; Fukugita & Turner 1991; Maoz & Rix 1993; Kochanek 1994, 1996). KKF also measured the evolution in the mass-to-light ratios of the lens galaxies with redshift and found results consistent with passive evolution models (e.g., Leitherer et al. 1996) and fundamental plane measurements in rich, high-redshift clusters (e.g., van Dokkum et al. 1998). These early results are based on limited observational samples.

The CASTLES project (CfA/Arizona Space Telescope Lens Survey) is a survey of known galaxy-mass lens systems using the *Hubble Space Telescope* (*HST*) and a uniform set of filters. Since the characteristic size of galaxy-scale lenses is $\Delta\theta \sim 1''$, precision photometric studies of the lensing galaxies are only practical with *HST*. Before CASTLES, *HST* images existed for about one-half of the ∼30 known galaxy-mass lens systems, but the diverse range of filters and exposure times that were used severely limited the usefulness of these observations (see KKF). The goals of CASTLES are (1) accurate astrometric measurements to refine lens models, particularly for systems where a time delay may provide a direct measurement of H_0; (2) photometric redshift estimates for all the lens galaxies in the sample, to sharpen lensing constraints on the cosmological constant Λ and galaxy evolution; (3) direct estimates of the M/L ratio of lens galaxies up to $z \sim 1$, to derive new constraints on their mean formation epoch and star formation history; (4) a comparison of the dark matter and stellar light distributions in the lens galaxies, and thus new constraints on the structure and shapes of galaxies; (5) measurements of the properties of the interstellar medium in distant galaxies, using differential extinction between the lensed images; (6) identification of as yet undetected lens galaxies in known multiple-image systems, which would confirm lensing and enlarge the sample for cosmological studies; (7) understanding of the environments of lens galaxies and their role in the lensing phenomenon; and (8) estimates of the photometric properties of the host galaxies of lensed quasars.

The survey consists of all ∼60 small-separation ($\Delta\theta < 10''$) gravitational lenses. The lenses were found as a produce of optical quasar surveys, radio lens surveys, and serendipity (see Kochanek 1993). In all cases, there is a dominant lens galaxy which may be a member of a group or

---

[2] Harvard-Smithsonian Center for Astrophysics, 60 Garden Street, Cambridge, MA 02138.

[3] Steward Observatory, University of Arizona, Tucson, AZ 85721.

[4] Max-Planck-Institut für Astronomie, Koenigstuhl 17, Heidelberg, D-69117, Germany.

[5] See http://cfa-www.harvard.edu/castles for a more complete summary.

small cluster. The heterogeneity of the overall sample is important for some questions (e.g., the separation distribution) but relatively unimportant for others (e.g., the evolution of the lens galaxies). We observed our targets in the near-infrared through the F160W (H band) filter with the NICMOS camera NIC2. In cases where the lens was expected to be very bright, we split the exposures to also include an F205W (K-band) exposure. The infrared observations are complemented by new or archival WFPC2 imaging in the F814W (I band), F675W (R band), or F555W (V band) to obtain uniform VIH or RIH multicolor photometry of the systems. When available, we have also analyzed archival NIC1 images.

In this paper, we restrict our attention to 10 two-image lens systems (Table 1). Detailed investigations of two-image lensed systems are limited by the small number of observational constraints. In many cases the contrast is too high, or the image separation is too small, to permit precise photometric modeling of the lens (B0218+357, SBS 0909+532, LBQS 1009−0252, Q1017−207, Q1208+1011 and PKS 1830−211). The CASTLES observations of four-image lenses will be presented in a later paper (McLeod et al. 2000, in preparation), and some individual targets with more constraints have been published (e.g., PG 1115+080, Impey et al. 1998; MG 1131+0456 Kochanek et al. 2000a). Surveys of the physical properties of the lenses are considered elsewhere, such as extinction (Falco et al. 1999), the fundamental plane (Kochanek et al.

2000b), and the properties of lensed quasar host galaxies (Rix et al. 1999, 2000, in preparation).

We start by outlining our general procedures for carrying out, reducing, and interpreting the observations. In § 2 we describe the data reduction, in § 3 the decomposition of the images into a photometric model, and in § 4 we describe the interpretation of the data using gravitational lens models. In § 5 we discuss the properties of the 10 systems analyzed in this paper, and in § 6 we summarize the results. An Appendix presents the data reduction procedures we have developed for NICMOS data.

2. OBSERVATIONS AND REDUCTION

Table 1 lists the available NICMOS and WFPC2 observations of the 10 lenses we consider. We acquired near-infrared imaging with the NICMOS/NIC2 camera, observing the targets for one-half, one, or two orbits using the H-band (F160W) filter. Whenever one-half of an orbit was sufficient, the remainder was used to obtain a K-band (F205W) image. For each target we obtained four dithered exposures to minimize the effects of detector defects and edges, and cosmic-ray persistence following South Atlantic Anomaly (SAA) passages. Initially, we used subarcsecond dithers, but experience with the first data sets showed that larger dithers ($\sim 4''$) allow for better background subtraction. The early HST pipeline image reductions were inadequate for performing accurate image modeling and photometry; therefore, we developed our own custom

TABLE 1

SUMMARY OF OBSERVATIONS

Target	Band = Camera/Filter	Time (s)	N/Dith	Detect	UT Date	Source
Q0142−100	H = NIC2/F160W	2560	4/1.1	22.5	1997.08.15	CASTLES
	R = WFPC2/F675W	2500	5/—	25.6	1994.11.22	KKF
	V = WFPC2/F555W	1200	3/—	25.5	1994.11.22	KKF
B0218+357	H = NIC1/F160W	7866	5/—	21.7	1997.08.07	Xanthopoulos et al. 1999
	H = NIC2/F160W	2560	4/0.6	23.7	1997.08.19	CASTLES
	I = WFPC2/F814W	1000	2/—	24.5	1995.07.22	Xanthopoulos et al. 1999
	V = WFPC2/F555W	1000	2/—	25.4	1995.07.22	Xanthopoulos et al. 1999
SBS 0909+523	H = NIC2/F160W	2816	4/7.9	22.9	1997.11.07	CASTLES
	I = WFPC2/F814W	640	4/1.1	23.5	1999.03.18	CASTLES
	V = WFPC2/F555W	640	4/1.1	24.5	1999.03.17	CASTLES
BRI 0952−0115	H = NIC2/F160W	5120	8/8.0	23.1	1997.10.17	CASTLES
	R = WFPC2/F675W	5400	3/—	25.5	1994.10.22	KKF
LBQS 1009−0252......	H = NIC2/F160W	2560	4/7.7	23.6	1997.11.15	CASTLES
	I = WFPC2/F814W	2600	2/—	24.6	1999.01.01	GO-6790, Surdej
	V = WFPC2/F555W	1600	4/0.4	24.8	1999.01.01	GO-6790, Surdej
Q1017−207	H = NIC2/F160W	2560	4/8.0	23.3	1997.11.14	CASTLES
	I = WFPC2/F814W	2300	6/2.3	24.8	1995.11.28	Remy et al. 1998
	V = WFPC2/F555W	800	5/2.3	24.7	1995.11.28	Remy et al. 1998
B1030+071	H = NIC1/F160W	2624	2/—	20.7	1997.11.20	GO-7255, Jackson
	I = WFPC2/F814W	1000	2/—	24.5	1997.02.03	Xanthopoulos et al. 1998
	V = WFPC2/F555W	1000	2/—	25.4	1997.02.03	Xanthopoulos et al. 1998
HE 1104−1805	H = NIC2/F160W	2560	4/7.9	22.9	1997.11.22	CASTLES
	I = WFPC2/F814W	1000	6/2.3	23.8	1995.11.19	Remy et al. 1998
	V = WFPC2/F555W	200	2/—	23.6	1995.11.19	Remy et al. 1998
Q1208+1011............	H = NIC2/F160W	2560	4/7.1	23.0	1997.08.15	CASTLES
	I = WFPC2/F814W	2400	6/1.0	24.4	1999.06.04	CASTLES
	V = WFPC2/F555W	2400	6/1.0	25.2	1999.06.04	CASTLES
PKS 1830−211.........	K = NIC2/F205W	1408	8/5.8	21.3	1997.10.31	CASTLES
	H = NIC2/F160W	3072	8/5.8	22.1	1997.10.31	CASTLES
	I = WFPC2/F814W	1600	4/1.0	23.2	1999.05.12	CASTLES

NOTES.—" N/Dith " refers to the number of exposures and largest dither separation (arcsec). The detection limit is the magnitude at which 50% of randomly added 0".3 FWHM Gaussians are found by SExtractor (see § 2).

TABLE 2

Nearby Objects

ID	R.A. (arcsec)	Decl. (arcsec)	R (mag)	V − R (mag)	R − H (mag)	γ_T	PA (deg)	Comments
Q0142−100:								
G1	2.9	−10.1	18.95 ± 0.10	0.99 ± 0.03	2.28 ± 0.03	0.079	−7	
G2	5.8	−2.5	22.70 ± 0.10	0.71 ± 0.05	2.05 ± 0.05	0.030	−64	
S1	−16.7	−9.8	23.98 ± 0.11	0.17 ± 0.06				
G3	4.5	−1.5	24.40 ± 0.14	>0.38	<2.62	0.021	−72	
G4	−1.3	9.5	24.76 ± 0.13	>0.47	<2.53	0.005	−17	
G5	7.6	11.0	25.00 ± 0.14	>0.69		0.004	27	
T1	−75.0	−13.2	17.36 ± 0.10	0.67 ± 0.03		0.020	81	
T2	−53.1	19.9	18.44 ± 0.10	0.87 ± 0.03		0.016	−70	
T3	−30.1	−58.5	19.09 ± 0.10	0.63 ± 0.03		0.011	29	

ID	R.A. (arcsec)	Decl. (arcsec)	I (mag)	V − I (mag)	I − H (mag)	γ_T	PA (deg)	Comments
B0218+357:								
G1	−11.7	−12.9	19.42 ± 0.10	1.22 ± 0.03		0.005	42	
G2	17.5	−8.9	22.17 ± 0.10	0.94 ± 0.05		0.001	−62	
G3	2.9	15.8	22.55 ± 0.11	2.74 ± 0.11		0.001	10	
G4	−7.3	−5.1	22.60 ± 0.12	>1.51	3.26 ± 0.07	0.002	55	
G5	−10.2	−1.9	23.10 ± 0.12	>2.32		0.002	79	
G6	3.8	8.8	23.19 ± 0.11	1.87 ± 0.10		0.002	23	
G7	−10.3	−11.2	23.55 ± 0.12	>1.67		0.001	43	
G8	15.2	0.9	23.56 ± 0.13	1.15 ± 0.11		0.001	87	
G9	2.0	4.1	23.67 ± 0.12	>1.73	2.81 ± 0.07	0.003	24	
G10	−8.5	−12.4	23.88 ± 0.15	>1.16		0.001	35	
G11	6.5	2.4	24.10 ± 0.13	>1.46	2.44 ± 0.08	0.002	70	
G12	−13.1	7.6	24.20 ± 0.14	1.29 ± 0.13		0.001	−60	
G13	2.5	14.2	24.35 ± 0.15	>1.40		0.001	9	
H1	−4.1	−6.4			>1.69	0.001	33	H = 22.13 ± 0.12
H2	6.6	−0.5			>0.91	0.001	−85	H = 23.59 ± 0.16

ID	R.A. (arcsec)	Decl. (arcsec)	I (mag)	V − I (mag)	I − H (mag)	γ_T	PA (deg)	Comments
SBS 0909+523:								
S1	13.7	7.0	17.18 ± 0.10	1.86 ± 0.03				
G1	−1.7	−1.7	21.49 ± 0.10	2.61 ± 0.08	2.43 ± 0.04	0.037	51	
G2	3.7	−0.2	22.57 ± 0.11	>1.74	2.30 ± 0.05	0.019	−87	
S2	4.3	−4.0	23.09 ± 0.11	>1.63	2.67 ± 0.05			
G3	−7.0	−5.3	23.33 ± 0.13	1.33 ± 0.12	1.59 ± 0.08	0.005	54	
H1	−7.3	−5.5			>1.59	0.003	55	H = 21.54 ± 0.11
H2	4.4	3.9			>1.69	0.004	46	H = 21.80 ± 0.10
H3	11.4	−3.7			>1.21	0.002	−71	H = 21.83 ± 0.11
H4	5.3	9.4			>1.67	0.002	28	H = 21.84 ± 0.11
H5	7.5	0.3			>1.02	0.003	87	H = 21.98 ± 0.11

ID	R.A. (arcsec)	Decl. (arcsec)	R (mag)	R − H (mag)	R − H (mag)	γ_T	PA (deg)	Comments
BRI 0952−0115:								
G1	15.6	10.5	21.80 ± 0.10			0.016	55	
G2	6.9	12.6	22.96 ± 0.10	3.29 ± 0.03		0.012	29	
G3	4.0	0.2	24.19 ± 0.11	1.71 ± 0.06		0.023	81	
G4	−0.1	−12.0	24.59 ± 0.12	3.02 ± 0.07		0.007	−2	
G5	15.5	−3.9	24.73 ± 0.12			0.005	−78	
G6	4.8	−9.5	24.84 ± 0.15			0.007	−30	
G7	10.9	−4.9	24.91 ± 0.12	2.79 ± 0.07		0.006	−69	
T1	38.0	−26.3	19.38 ± 0.10			0.020	−56	
T2	−12.2	−31.3	20.70 ± 0.10			0.016	21	
T3	26.9	9.4	21.40 ± 0.10			0.013	70	

TABLE 2—*Continued*

ID	R.A. (arcsec)	Decl. (arcsec)	H (mag)	V−I (mag)	I−H (mag)	γ_T	PA (deg)	Comments
LBQS 1009−0252:								
S1 = C	−4.3	1.7	18.69 ± 0.10	0.90 ± 0.03	0.85 ± 0.03	∼0.08	−53	Shear from C′
S2	−0.9	−7.7	22.44 ± 0.10	1.60 ± 0.05	1.10 ± 0.04			
G1	−6.8	−7.4	22.62 ± 0.10	>1.92	2.86 ± 0.04	0.034	44	
G2	6.0	8.5	22.67 ± 0.11	1.55 ± 0.09	2.03 ± 0.05	0.025	34	
G3	−4.2	7.5	23.08 ± 0.11	>2.00	1.24 ± 0.07	0.026	−23	
G4	−5.3	11.4	23.19 ± 0.11	>1.84	1.87 ± 0.05	0.017	−21	
G5	10.3	−15.9	23.24 ± 0.12	>1.16		0.012	−36	
G6	−4.3	−5.9	24.04 ± 0.12	>1.03	1.41 ± 0.09	0.025	38	
G7	−5.0	−12.3	24.48 ± 0.12	0.41 ± 0.08	<2.33	0.011	22	
G8	8.4	−10.7	24.67 ± 0.13	>0.20		0.009	−43	
H1	3.9	−2.4			>1.18	0.023	−73	H = 22.60 ± 0.12
T1	26.0	24.4	17.88 ± 0.10	1.17 ± 0.03		0.072	46	
T2	101.8	−64.4	18.04 ± 0.10	2.09 ± 0.03		0.020	−58	

ID	R.A. (arcsec)	Decl. (arcsec)	I (mag)	V−I (mag)	I−H (mag)	γ_T	PA (deg)	Comments
Q1017−207:								
S1	9.3	1.7	19.67 ± 0.10	1.59 ± 0.03	1.92 ± 0.03			
S2	5.5	14.8	22.90 ± 0.10	>1.89	<−0.49			
G1	3.7	2.6	23.06 ± 0.12	>1.64	2.47 ± 0.05	0.026	59	
G2	5.7	−13.5	23.07 ± 0.12	1.05 ± 0.16	<0.73	0.009	−25	
G3	6.7	−14.2	23.32 ± 0.11	0.62 ± 0.08		0.007	−27	
G4	2.6	14.9	24.19 ± 0.13	0.96 ± 0.14		0.005	12	
H1	2.4	−7.9			>1.42	0.005	−21	H = 22.51 ± 0.13
T1	−5.0	−43.1	18.84 ± 0.10	1.28 ± 0.03		0.021	6	
T2	−9.1	−52.6	18.86 ± 0.10	2.16 ± 0.03		0.017	9	
T3	4.0	−37.2	19.72 ± 0.10	2.42 ± 0.04		0.017	−7	
T4	18.8	−16.1	20.45 ± 0.10	2.46 ± 0.04		0.018	−50	

ID	R.A. (arcsec)	Decl. (arcsec)	I (mag)	V−I (mag)	I−H (mag)	γ_T	PA (deg)	Comments
B1030+071:								
G1	−8.9	7.4	19.63 ± 0.10	0.90 ± 0.03		0.044	−49	
G2	−10.5	−8.9	22.79 ± 0.11	>2.67		0.010	55	
G3	−1.1	2.4	23.57 ± 0.14	>1.33	<3.37	0.023	−30	
G4	−2.5	3.4	23.91 ± 0.12	0.88 ± 0.08	<2.95	0.014	−37	
G5	0.3	5.6	24.00 ± 0.13	1.18 ± 0.12		0.011	−5	
G6	2.7	−4.9	24.20 ± 0.15	1.58 ± 0.19	3.69 ± 0.12	0.016	−26	
G7	5.8	−2.9	24.25 ± 0.14	>1.24	<3.46	0.013	−70	

ID	R.A. (arcsec)	Decl. (arcsec)	I (mag)	V−I (mag)	I−H (mag)	γ_T	PA (deg)	Comments
HE 1104−1805:								
S1	−3.6	−15.1	17.51 ± 0.10	1.36 ± 0.03	<−5.42			
G1	−3.1	4.6	21.89 ± 0.11	0.78 ± 0.08	1.45 ± 0.04	0.048	−38	
T1	73.2	−43.7	19.17 ± 0.10	2.59 ± 0.04		0.013	−59	
T2	−4.3	−59.5	19.40 ± 0.10	0.82 ± 0.03		0.017	5	
T3	−28.5	−42.5	19.79 ± 0.10	1.29 ± 0.05		0.016	35	
T4	22.9	−42.1	20.41 ± 0.10	0.74 ± 0.04		0.013	−28	

ID	R.A. (arcsec)	Decl. (arcsec)	I (mag)	V−I (mag)	I−H (mag)	γ_T	PA (deg)	Comments
Q1208+1011:								
G1	−3.8	18.8	20.77 ± 0.10	0.94 ± 0.03		0.037	−11	
G2	−0.5	−9.3	21.57 ± 0.10	1.06 ± 0.04	1.43 ± 0.04	0.054	3	
G3	−6.9	−7.7	22.80 ± 0.11	1.26 ± 0.06	1.57 ± 0.06	0.028	43	
G4	−12.4	2.7	23.95 ± 0.12	0.77 ± 0.06	2.27 ± 0.06	0.013	−77	
G5	9.1	16.7	24.22 ± 0.13	>1.26		0.008	28	
G6	−4.5	14.5	24.26 ± 0.13	0.84 ± 0.08		0.009	−17	
H1	−8.6	0.3			>1.58	0.020	−86	H = 21.34 ± 0.11

TABLE 2—*Continued*

ID	R.A. (arcsec)	Decl. (arcsec)	H (mag)	$I-H$ (mag)	$H-K$ (mag)	γ_T	PA (deg)	Comments
PKS 1830−211:								
G1	−8.9	7.4	19.63 ± 0.10	0.90 ± 0.03		0.044	−49	
G2	−10.5	−8.9	22.79 ± 0.11	>2.67		0.010	55	
G3	−1.1	2.4	23.57 ± 0.14	>1.33	<3.37	0.023	−30	
G4	−2.5	3.4	23.91 ± 0.12	0.88 ± 0.08	<2.95	0.014	−37	
G5	0.3	5.6	24.00 ± 0.13	1.18 ± 0.12		0.011	−5	
G6	2.7	−4.9	24.20 ± 0.15	1.58 ± 0.19	3.69 ± 0.12	0.016	−26	
G7	5.8	−2.9	24.25 ± 0.14	>1.24	<3.46	0.013	−70	

NOTES.—T (mag) § 2. F (mag)$I = 23$ and $H = 21$. The coordinate origin is the "A" image of the lens. The standard catalog of objects extends to a radius of 20″ from the lens, with objects labeled G# for galaxies and S# for stellar objects, respectively. Galaxies outside the 20″ radius which could produce a tidal shears exceeding 1% are labeled by T#. Objects labeled H# were detected only in the infrared. Tidal shear estimates are scaled to the lens galaxy magnitude in the corresponding filter, after correcting for the SExtractor magnitude offset discussed in § 2. For Q1208+1011, where we did not detect the lens galaxy, γ_T estimates assume lens magnitudes of $I = 23$ and $H = 21$.

package "NICRED," based on C programs and IRAF[6] routines (McLeod 1997). As it is applicable to many other NICMOS data sets, we describe our reduction in the Appendix. The archival NICMOS/NIC1 images were reduced using the same methods, but with significantly poorer results because they were not dithered and there were not enough data to construct sky darks.

We reduced new or archival WFPC2 images of the systems in a manner similar to the last steps of NICRED. We ignored archival WFPC1 images of the lenses because the extended point spread function (PSF) skirts of the bright quasars generally obscured the properties of the lens galaxy. We first produced shifted subimages for each exposure, as in NICRED, using a 3 σ "ccdclip" rejection algorithm (or 3 σ "crreject" in cases where there were fewer than four exposures on a target). This rejection removed nearly all the cosmic rays from the combined images. The combined images were then averaged together with exposure-time weighting. Many hot pixels and chip defects remain in the final images created from undithered archival observations.

We use Vega-referenced magnitudes for the *HST* filters used in the observations. The NICMOS calibration was determined by fitting PSF models to observations of the standard star P330E and then referencing to ground-based photometry (Persson et al. 1998). The transformations from ground-based filters to the NICMOS filters were done synthetically. The resulting zero-point magnitudes (for 1 count s^{-1} in an infinite aperture) are 21.88, 21.80, and 22.47, respectively, for the F205W, F160W, and F110W filters. The WFPC2 calibrations are from Holtzman et al. (1995) after changing to a gain of 7 and correcting from a finite aperture to an infinite aperture (~ 0.1 mag), as needed for our fitting procedures. The zero-point magnitudes we applied are 21.69 for F814W; 22.08 for F675W; and 22.57 for F555W. We refer to the F555W, F675W, F814W, F110W, F160W, and F205W bands as V, R, I, J, H, and K, respectively. We estimate the uncertainty in the zero points to be ~ 0.05 mag.

We used the SExtractor package (Bertin & Arnouts 1996) to catalog the objects found in the NICMOS and WFPC2 fields. We present the catalogs for all our targets in Table 2. The objects were morphologically classified as galaxies or

stellar by SExtractor, followed by visual confirmation. In ground-based images, SExtractor classification accuracy depends on seeing and image depth but is typically $\sim 90\%$ accurate for objects more than 1 mag brighter than the detection limit. The total object magnitudes were estimated using Kron-type (Bertin & Arnouts 1996) automatic apertures. We tested the galaxy photometry by adding ~ 100 synthetic galaxies to WFPC2 and NICMOS images, and measuring them using our procedure. SExtractor accurately determined the magnitudes for objects with Gaussian profiles, but systematically underestimated the flux for de Vaucouleurs and exponential profile galaxies. The effect varied with the size of the galaxy and the PSF, and for a typical de Vaucouleurs R_e of 0″.3, the shift was $\approx 0.1 \pm 0.2$ and $\approx 0.5 \pm 0.2$ mag for the WFPC2 and NICMOS chips, respectively. The quoted photometric uncertainties are a quadrature sum of the scatter in this systematic shift and the internal SExtractor uncertainties. Galaxy colors were determined within fixed circular apertures (0″.3, 0″.56, 1″.0, or 1″.7), with results given for the smallest aperture whose diameter exceeds $\sqrt{2}$ times the mean object major diameter in the deepest optical exposure. We used synthetic PSF models (see § 3) to determine that PSF color terms are $\lesssim 0.02$ mag, sufficiently small to be ignored for these galaxy colors. We estimated our detection limits by randomly adding 0″.3 FWHM Gaussians to each field and determining the magnitude at which 50% are detected by SExtractor. We first cataloged all objects within 20″ of the lens based on the deepest optical image (galaxies and stars labeled with "G" and "S," respectively, in order of decreasing brightness). We then added any galaxies detected only in the H-band images (labeled with "H") and more distant galaxies which could tidally influence the lens system (labeled with "T," see § 4).

3. IMAGE DECOMPOSITION

The angular extent of a lens galaxy is usually comparable to the angular separation of the images that it produces, so the data consist of overlapping images of objects at different redshifts. This problem is compounded by the fact that the angular separations of components are also comparable to the size of the *HST* point spread function. A successful analysis therefore requires a rigorous simultaneous image decomposition into source and lens components.

Both the WFPC2 and NICMOS point-spread functions (PSF) consist of a sharp central core (FWHM ~ 0″.1), the

TABLE 3

PHOTOMETRY AND ASTROMETRY

Lens	ID	z	R.A. (arcsec)	Decl. (arcsec)	Magnitude (mag)	Color1 (mag)	Color2 (mag)	Color3 (mag)	R_e (arcsec)	$1-b/a$	PA (deg)	Comments
Q0142−100	A	2.72	$\equiv 0$	$\equiv 0$	$H=15.28\pm0.02$	$V-R=0.22\pm0.11$	$V-H=1.61\pm0.09$	$R-H=1.39\pm0.06$				
	B	2.72	2.145 ± 0.003	-0.613 ± 0.003	$H=17.57\pm0.03$	$V-R=0.17\pm0.05$	$V-H=1.56\pm0.05$	$R-H=1.39\pm0.04$				
	G	0.49	1.764 ± 0.003	-0.574 ± 0.003	$H=16.63\pm0.03$	$V-R=1.46\pm0.02$	$V-H=4.18\pm0.03$	$R-H=2.72\pm0.02$	0.59 ± 0.03	0.25 ± 0.02	61 ± 4	DV
B0218+357	A	0.96	$\equiv 0$	$\equiv 0$	$H=17.52\pm0.03$	$V-I=1.45\pm0.24$	$V-H=5.76\pm0.21$	$I-H=4.31\pm0.11$				
	B	0.96	0.307 ± 0.003	0.126 ± 0.003	$H=16.94\pm0.03$	$V-I=1.72\pm0.07$	$V-H=4.17\pm0.06$	$I-H=2.45\pm0.04$				
	G	0.68	0.181 ± 0.03	0.069 ± 0.03	$H=17.50\pm0.04$	$V-I=1.89\pm0.34$	$V-H=4.45\pm0.29$	$I-H=2.56\pm0.19$	0.19 ± 0.01	$\equiv 0$	...	ED
SBS 0909+523	A	1.38	$\equiv 0$	$\equiv 0$	$H=14.60\pm0.02$	$V-I=0.69\pm0.26$	$V-H=2.16\pm0.26$	$I-H=1.47\pm0.02$				
	B	1.38	0.987 ± 0.003	-0.498 ± 0.003	$H=14.73\pm0.03$	$V-I=1.24\pm0.15$	$V-H=2.93\pm0.14$	$I-H=1.69\pm0.05$				
	G	0.83	0.415 ± 0.141	-0.004 ± 0.082	$H=16.75\pm0.74$	$V-I>1.4$	$V-H>3.2$	$I-H=2.29\pm0.80$	1.58 ± 0.90	$\equiv 0$	...	DV
BRI 0952−0115......	A	4.50	$\equiv 0$	$\equiv 0$	$H=17.07\pm0.02$	$R-H=2.13\pm0.02$						
	B	4.50	-0.696 ± 0.003	-0.709 ± 0.003	$H=18.44\pm0.02$	$R-H=2.04\pm0.04$						
	G	(0.41)	-0.396 ± 0.003	-0.506 ± 0.003	$H=18.95\pm0.16$	$R-H=3.13\pm0.05$			0.14 ± 0.05	0.47 ± 0.05	59 ± 4	DV
LBQS 1009−0252...	A	2.74	$\equiv 0$	$\equiv 0$	$H=16.63\pm0.02$	$V-I=0.52\pm0.04$	$V-H=1.84\pm0.04$	$I-H=1.32\pm0.04$				
	B	2.74	-0.670 ± 0.003	-1.383 ± 0.003	$H=18.20\pm0.04$	$V-I=1.05\pm0.06$	$V-H=2.85\pm0.06$	$I-H=1.80\pm0.05$				
	G	(0.82)	-0.537 ± 0.003	-1.097 ± 0.003	$H=19.26\pm0.14$	$V-I>2.1$	$V-H>4.7$	$I-H=2.63\pm0.06$	0.19 ± 0.04	$\equiv 0$	...	DV
	G'		0.289 ± 0.003	-0.570 ± 0.003	$H=19.67\pm1.13$				0.99 ± 1.17	$\equiv 0$	...	DV Nearby galaxy
	C	1.63	-4.297 ± 0.004	1.624 ± 0.003	$H=17.91\pm0.04$	$V-I=0.53\pm0.06$	$V-H=1.28\pm0.06$	$I-H=0.75\pm0.02$	$\equiv 0.6$	$\equiv 0$	...	Quasar 2
	C'	1.63	-4.277 ± 0.092	1.568 ± 0.044	$H=19.21\pm0.22$							DV Quasar 2 host
Q1017−207	A	2.55	$\equiv 0$	$\equiv 0$	$H=15.66\pm0.03$	$V-I=0.51\pm0.04$	$V-H=1.77\pm0.04$	$I-H=1.26\pm0.04$				
	B	2.55	-0.847 ± 0.003	0.027 ± 0.003	$H=17.81\pm0.05$	$V-I=0.51\pm0.13$	$V-H=1.77\pm0.14$	$I-H=1.26\pm0.06$				
	G	(0.77)	-0.659 ± 0.016	0.016 ± 0.017	$H=19.26\pm0.06$	$V-I>1.1$	$V-H>3.7$	$I-H=2.56\pm0.49$	$\equiv 0.30$	$\equiv 0$	...	DV
B1030+071	A	1.54	$\equiv 0$	$\equiv 0$	$I=19.04\pm0.03$	$V-I=1.17\pm0.04$	$V-H=4.33\pm0.03$	$I-H=3.16\pm0.04$				
	B	1.54	0.928 ± 0.003	-1.257 ± 0.003	$I=22.09\pm0.09$	$V-I=1.17\pm0.09$	$V-H=3.57\pm0.11$	$I-H=2.40\pm0.11$				
	G	0.60	0.841 ± 0.011	-1.088 ± 0.003	$I=20.16\pm0.05$	$V-I=2.56\pm0.04$	$V-H=5.07\pm0.21$	$I-H=2.51\pm0.21$	0.48 ± 0.02	0.22 ± 0.04	28 ± 24	DV
	G'		0.353 ± 0.021	-1.231 ± 0.020	$I=22.35\pm0.23$	$V-I=2.31\pm0.37$	$V-H=5.47\pm0.51$	$I-H=3.16\pm0.36$	0.11 ± 0.02	$\equiv 0$	...	ED
HE 1104−1805	A	2.32	$\equiv 0$	$\equiv 0$	$H=15.57\pm0.03$	$V-I=0.40\pm0.06$	$V-H=1.21\pm0.06$	$I-H=0.81\pm0.05$				
	B	2.32	2.901 ± 0.003	-1.332 ± 0.003	$H=17.04\pm0.04$	$V-I=0.59\pm0.06$	$V-H=1.56\pm0.05$	$I-H=0.97\pm0.06$				
	G	(0.77)	0.974 ± 0.003	-0.510 ± 0.004	$H=17.47\pm0.27$	$V-I>3.0$	$V-H>5.5$	$I-H=2.54\pm0.11$	0.73 ± 0.24	0.23 ± 0.05	63 ± 17	DV
Q1208+101	A	3.80	$\equiv 0$	$\equiv 0$	$H=15.91\pm0.03$	$V-I=1.20\pm0.10$	$V-H=2.51\pm0.10$	$I-H=1.31\pm0.04$				
	B	3.80	0.127 ± 0.003	-0.461 ± 0.003	$H=17.55\pm0.02$	$V-I=1.03\pm0.09$	$V-H=2.11\pm0.04$	$I-H=1.08\pm0.09$				
PKS 1830−211	A	2.51	$\equiv 0$	$\equiv 0$	$H=16.94\pm0.02$	$I-H=5.35\pm0.07$	$I-K=6.86\pm0.07$	$H-K=1.51\pm0.02$				
	B	2.51	-0.653 ± 0.003	-0.721 ± 0.003	$H=22.43\pm0.35$	$I-H>3.6$	$I-K>6.6$	$H-K=3.00\pm0.39$				
	G	0.89	-0.501 ± 0.075	-0.445 ± 0.080	$H=18.58\pm0.39$	$I-H=2.84\pm0.26$	$I-K=4.02\pm0.13$	$H-K=1.18\pm0.25$	0.40 ± 0.08	$\equiv 0$	...	ED
	P		-0.315 ± 0.006	-0.464 ± 0.004	$H=21.41\pm0.13$	$I-H=2.61\pm0.26$	$I-K=3.77\pm0.35$	$H-K=1.16\pm0.30$				
	S1		0.088 ± 0.003	0.535 ± 0.003	$H=17.10\pm0.02$	$I-H=2.31\pm0.05$	$I-K=2.71\pm0.05$	$H-K=0.40\pm0.02$				M star

NOTES.—ED: Exponential disk. DV: de Vaucouleurs. Redshifts in parentheses are estimates based on the fundamental plane of gravitational lens galaxies (Kochanek et al. 2000). The magnitude uncertainties (sixth column) are derived while fitting the photometric structure of the galaxy (R_e, $1-b/a$, PA), whereas the color uncertainties (seventh, eighth, and ninth columns) are determined for a fixed photometric structure.

first Airy ring, and an outer skirt of low intensity ($\leq 1\%$ of the peak intensity) with a complex spatial variation in azimuth. For models of the WFPC2 and NIC1 data we used TinyTim v4.4 (Krist & Hook 1997) model PSFs taking into account the location of the object and, for the NIC1 data, the position of the Pupil Alignment Mechanism. For models of the NIC2 data we used a set of 13 stellar images (McLeod, Rieke, & Storrie-Lombardi 1999). The empirical PSF images were reduced exactly like the images of the lenses. When we fitted the PSFs to isolated stellar sources, the peak residuals were less than 2% of the peak intensity of the source and the rms residuals integrated over the PSF were less than 1% of the total flux. The systematic residuals are due to the time variability of the PSF as NICMOS lost coolant, as well as to the limited temporal and spatial sampling of the available PSFs. We fitted each lensed system using all the empirical PSFs in our library and selected as a reference that model whose PSF yielded the best fit to the observed data. Which PSF provided the best fit did not correlate with observation time or position on the sky.

We used parameterized models to separate lens and source components: in most cases, the source images were assumed to be unresolved and the lens galaxies were described by ellipsoidal exponential disk or de Vaucouleurs models. Thus, a typical model for a two-image lens system is specified by 12 parameters: the position and flux of each point source, and the position, flux, major axis scale length, axis ratio, and position angle (PA) of the lens galaxy. Where necessary, we included additional parameters to model the background level and an empirical Gaussian blur to improve the PSF match. The model, convolved with the PSF, was fitted to the image by adjusting its parameters to minimize the sum of the squared residuals, using Powell's algorithm (Press et al. 1988, pp. 309–317). The residuals are dominated by systematic deviations created by the PSF models, rather than statistical uncertainties. Therefore, we weighted the pixels uniformly in computing the χ^2 during the fit optimization. Changes in the weighting had little effect on the results. Parameter uncertainties were determined by combining three terms in quadrature: (1) a statistical error estimated from the parameter range found from separate fits to the individual exposures; (2) a PSF modeling error term from the range of parameters found from using different PSF models; and (3) a modeling term found from using two independent image fitting programs. The lens galaxy structure was determined from the filter with the highest signal-to-noise for the lens galaxy (usually the NIC2 H image, but the WFPC2 I image for B1030+074) and the galaxy structure was then held fixed for the fits to the other filters. Tests on several of the brightest early-type lenses in our sample showed no significant structural parameter differences between independent fits to the various filters. We did find some structural color dependence for late-type lenses, but both late-type lenses in this paper are too faint for this effect to be measurable. When we could not estimate galaxy scale lengths or axis ratios from our data, we assumed modest, fixed scale lengths and a round galaxy. The uncertainties in the galaxy colors were estimated with the photometric structure of the galaxy held fixed. The results of the photometric fits are presented in Table 3.

For the NIC2 images we fitted the model components on the two-times oversampled grid generated by NICRED, while for the NIC1 and WFPC2 data we fitted the data on

the original pixels. For the WFPC2 data we used a two-times oversampled PSF model. We assumed pixel scales of $0\rlap{.}''04554$ (Holtzman et al. 1995) for the PC1 images. We adopt pixel scales of $0\rlap{.}''076030$ and $0\rlap{.}''075344$ for the x- and y-axes of NIC2, and $0\rlap{.}''043230$ and $0\rlap{.}''043056$ for NIC1.[7] We verified the astrometric accuracy of our fits through cross checks between the different detectors and against VLBI positions for the images in B0218+357 (difference $= 2.0 \pm 1.0$ mas), B1030+074 (6 ± 3 mas), and PKS 1830$-$211 (1 ± 4 mas). We impose a conservative minimum positional rms uncertainty of 3 mas for all objects.

4. LENS MODELING

After the images are decomposed into components, we can interpret the image geometry with a lens model. The most likely contributors to gravitational lensing are the principal lensing galaxy (which can be described by a central position, the mass within the Einstein ring radius, and the lens ellipticity and orientation), the tidal effects of nearby galaxies, which can usually be approximated by an external shear and its orientation, and the tidal effects produced by large-scale structure along the ray path.

4.1. *The Main Lens Galaxy*

Previous studies of lenses (e.g., Kochanek 1995), stellar dynamics (e.g., Rix et al. 1997) and X-ray studies (e.g., Fabbiano 1989) all suggest that the isothermal radial mass distributions ($\rho \propto 1/r^2$) are realistic representations of the total mass. Other lens models that have traditionally been used (e.g., ellipsoidal modified Hubble models, Plummer models, or the more general power law surface density $\Sigma \propto [R^2 + S^2]^{-\alpha}$) are known to be unphysical—we know that the central regions of galaxies are cuspy and do not have homogeneous cores (e.g., Faber et al. 1997). Therefore, the centers of lens models should be described by a density cusp $\rho \propto r^{-a}$ with $1 \lesssim a \lesssim 2$ for $r \ll 1$. For the isothermal model $a = 2$, for the de Vaucouleurs model $a \simeq 1.25$, and $a = 1$ for the Hernquist (1990) or NFW models (Navarro, Frenk, & White 1996). A radial scale for these models is specified by the "break radius" between the inner cusp and a steeper outer profile. In dark matter models the break radius is sufficiently large compared to the size of the lens to be ignored (see Navarro, Frenk, & White 1996), while in constant M/L models it is comparable to the effective radius.

We consider three standard lens models. The singular isothermal ellipsoid (SIE), the de Vaucouleurs model, and the exponential disk. The surface density of the SIE in units of the critical surface density for lensing is

$$\kappa(x, y) = \frac{b}{2} \left[\frac{2q^2}{1 + q^2} (x^2 + y^2/q^2) \right]^{-1/2}, \qquad (1)$$

where q is the axis ratio, and b would be the critical radius for a singular isothermal sphere ($q \equiv 1$). In cases where we have a good photometric model of the lens galaxy we also consider constant mass-to-light ratio (M/L) models where the lensing mass distribution matches the light distribution of the observed galaxies, for most cases a de Vaucouleurs profile. The scaled surface density of the de Vaucouleurs

---

[7] http://www.stsci.edu/instruments/nicmos/nicmos_doc_platescale.html.

model is defined by

$$\kappa(x, y) = \frac{b}{2\mathcal{N} r_e} \exp\left[-k\left(\frac{x^2 + y^2/q^2}{r_e^2}\right)^{1/8}\right], \qquad (2)$$

where r_e is the major-axis effective radius, $k = 7.67$, and $\mathcal{N} = \int_0^\infty v e^{-kv^{1/4}} dv$. To model spiral galaxies, we used an exponential disk model, with

$$\kappa(x, y) = \frac{b}{q} \exp\left(-\frac{\sqrt{x^2 + y^2/q^2}}{R_d}\right), \qquad (3)$$

where R_d is the scale length and b sets the mass scale. The axis ratio is $q = |\sin i|$ for a thin disk at inclination angle i ($i = 0$ for edge-on). Although none of the late-type galaxies in this paper have sufficient signal to determine q, we will use $q \neq 1$ models elsewhere. A lens model consisting of an isolated exponential disk usually produces a third or central image that is never observed in real lenses, making it an unacceptable model if used by itself (Keeton & Kochanek 1998). A third image can be suppressed by adding a more singular bulge or halo component.

4.2. External Shear from Nearby Galaxies

At some level, all gravitational lenses are perturbed by the tidal gravity produced by nearby galaxies or other mass concentrations. Keeton et al. (1997) found that every four-image system they considered required two quadrupole axes to obtain a good fit, independent of the choice for the radial mass distribution. The two axes are presumably the axis of the mean mass distribution of the primary lens galaxy and the axis of the mean tidal gravity field, although misaligned dark-matter halos are also possible. Thus, realistic models for any lens must include an external shear field.

We used the SExtractor catalogs (see § 2) to estimate the local tidal fields produced by nearby galaxies. We assumed that each nearby galaxy has an SIS mass distribution, the same M/L as the lens (after adjusting for the SExtractor magnitude offset for de Vaucouleurs galaxies, see § 2) and lies at the lens redshift. While the neighbors can be at different redshifts, affecting the estimated shears, we cannot make reliable photometric redshift and type estimates for the neighboring galaxies with the limited data available. For a primary lens with a critical radius of b_l, luminosity L_l, and a

neighbor at distance r_n with luminosity L_n, the Faber-Jackson relationship combined with the SIS lens model predicts a shear and convergence of $\gamma_T = \kappa_T = (1/2)(b_l/r_n)(L_n/L_l)^{1/2}$, if the neighbor's mass distribution extends to the lens system.[8] The 20″ cutoff radius for our standard catalog encompasses halo sizes of $\sim 100 \, h_{60}^{-1}$ kpc for $z_l \gtrsim 0.3$. However, if the dark halos of galaxies extend to $300 \, h_{60}^{-1}$ kpc (see, e.g., Zaritsky 1994), then galaxies up to $\sim 1'$ from the lens could have significant tidal effects. For this reason our field catalogs include distant, luminous galaxies whose estimated shears exceed 1% (the entries labeled with "T"). The halo truncation radius a is crucial for determining the influence of distant galaxies on the primary lens—a halo with critical radius b and a truncation radius a produces shear $\gamma_T = b/2r$ for radii $r \ll a$ and ba/r^2 for radii $r \gg a$ (see Brainerd, Blandford, & Smail 1996). Differences in the galaxy types affect the shear estimates because the mass-to-light ratios of late type galaxies are roughly 3 times lower than those of early-type galaxies, and the shear estimates are proportional to $\gamma_T \propto (M/L)^{1/2}$.

The total shear γ_T and convergence κ_T (see Table 4) are found by taking the tensor sum of the individual contributions. The convergence terms simply add, while the shear terms can cancel, so the totals for the two terms will differ. In the absence of detailed information on the redshifts and mass-to-light ratios of the neighbors, these estimates should be viewed as a qualitative picture of the strength and orientation of the tidal perturbations for each lens. For comparison we also include the shear $\gamma_{M/L}$ expected for galaxies without dark matter by computing the shear with the halos truncated at the lens critical radius ($a = b$). Without dark matter, neighboring galaxies produce negligible tidal perturbations.

4.3. Large-Scale Structure Shear

To the extent that all the neighboring galaxies are clustered at the lens redshift, our local tidal shear estimate is only a partial accounting of the sources of tidal pertur-

[8] We define the sign of the shear such that for a perturbing galaxy G_T, the PA of its shear matches the PA of a vector extending from the lens galaxy to G_T (modulo 180°). If a lens is modeled as an isothermal sphere with an external shear, the PA of the shear defined in this way will match the major axis PA of an equivalent isothermal ellipsoid model.

TABLE 4

TIDAL SHEAR ESTIMATES

	FIELD TOTAL			LARGEST			REMAINDER				
LENS	κ_T	γ_T	PA (deg)	κ_T	γ_T	PA (deg)	κ_T	γ_T	PA (deg)	$\gamma_{M/L}$	COSMIC γ_{LSS}
Q0142−100	0.138	0.072	−24.6	0.079	0.079	−6.8	0.060	0.047	−64.6	0.011	0.04
B0218+357	0.023	0.014	44.7	0.005	0.005	42.5	0.018	0.009	46.0	0.000	0.02
SBS 0909+523	0.075	0.057	62.6	0.037	0.037	51.3	0.038	0.027	78.8	0.003	0.03
BRI 0952−0115	0.081	0.027	72.3	0.026	0.026	87.2	0.055	0.014	37.3	0.002	0.05
LBQS 1009−0252......	0.261	0.053	−36.1	0.080	0.080	−53.3	0.182	0.047	16.9	0.010	0.04
Q1017−207	0.053	0.011	29.0	0.026	0.026	59.4	0.026	0.023	−18.7	0.001	0.04
B1030+071	0.131	0.093	−39.3	0.044	0.044	−48.9	0.087	0.053	−31.4	0.006	0.03
HE 1104−1805	0.048	0.048	−38.5	0.048	0.048	−38.5	0.000	0.000	0.0	0.005	0.04
Q1208+1011............	0.169	0.072	5.1	0.055	0.055	3.5	0.114	0.017	10.0	0.008	0.05
PKS 1830−211	0.158	0.096	−20.5	0.094	0.094	−18.9	0.064	0.006	−56.3	0.019	0.04

NOTES.—The *field total* shear and convergence from all the objects within 20″ of the lens (see Table 3). The total is broken down into the *largest* contribution from a single galaxy, and the *remainder* from all other galaxies. We show the convergence κ_T, and for the shear we give the magnitude γ_T and its orientation P(mag)§ 2). If the nearby galaxies have constant M/L, then the total shear, $\gamma_{M/L}$, is much smaller. The cosmological shear γ_{LSS} estimates the variance in the shear produced by perturbations along the rays.

bations, because potential fluctuations from large-scale structure along the ray path also contribute to the lens optics (Bar-Kana 1996). Although their full effects are more complicated than a simple external shear (see Bar-Kana 1996), their overall strength can be characterized by an effective shear γ_{LSS}. In general, the perturbations from other galaxies at the lens redshift are more important (see Keeton et al. 1997), but not by a large amount. Unfortunately, if $\gamma_T \sim \gamma_{LSS}$ we should see little correlation between the locations of nearby galaxies and the orientations of the external shear perturbations needed to model the lens. On the other hand, Keeton et al. (1997) noted that most of the cosmic or large-scale structure shear was generated by the nonlinear parts of the power spectrum which correspond to regions that collapse and produce halos filled with galaxies. This means that galaxies with small projected separations but different redshifts from the lens galaxy may be a reasonable tracer of the strength and orientation of γ_{LSS}. For each lens we used the semianalytic results in Keeton et al. (1997) to estimate the LSS shear expected for each lens (see Table 4).

4.4. The Standard Lens Models

Based on these physical considerations, we selected a set of four standard models to fit to all lens systems: (1) a dark matter model (the SIE model), (2) a model based on the photometric fits (the constant M/L model), (3) the dark matter model in an external shear field (the SIE + γ model), and (4) the photometric model in an external shear field (the $M/L + \gamma$ model). The lens models are fit to each lens system using the astrometric and structural properties from Table 3, augmented by more accurate VLBI data for the component separations when available. We used either the extinction-corrected optical flux ratios from Falco et al. (1999) or the observed radio flux ratios. The accuracy of flux ratio measurements is dominated by systematic problems (e.g., time variability or microlensing) rather than measurement precision, so we assumed a conservative minimum flux uncertainty of 5% per component. Time delays were computed in a flat $\Omega_0 = 1$ cosmology, using the lens redshift estimates from Kochanek et al. (2000b) where they had not been measured spectroscopically. In the M/L models we fixed the scale length, axis ratio, and position angle of the lens to the values found in the best-fit photometric model.[9]

For two-image lenses we usually have a total of five constraints on the lens model: the positions of the two images relative to the lens and the flux ratio of the images. Where we lack complete information on the lens properties we fit only the SIE model. Parameter uncertainties were estimated from the range over which $\Delta\chi^2 < 1$. For underconstrained models we surveyed the solution space and present allowed parameter ranges defined by the region with $\Delta\chi^2 < 1$. The SIE + γ model is highly underconstrained for a two-image lens, so we fixed the orientation of the SIE to that of the light, limited its ellipticity to be no larger than that of the light, and limited the external shear to be no more than twice the total environmental estimate (γ_T or γ_{LSS} from Table 4). The $M/L + \gamma$ models required no additional con-

straints since the shape and orientation of the galaxy are fixed.

5. RESULTS

Images of the 10 two-image lenses are shown in Figure 1, where we show the original image and the residual image found after modeling and subtracting the bright, lensed point sources. Figure 2 shows detailed images of the lensed quasar host galaxies found in BRI 0952−0115 and HE 1104−1805. Table 1 summarizes the data available for each system, and the results of the analyses described in §§ 2, 3, and 4 are presented in Tables 2–5. Table 2 presents the SExtractor catalogs for each surrounding field. Table 3 presents the source and lens components for each target. Table 4 gives the tidal shear estimates for each field, and Table 5 presents the lens models for each system. Figures 3 and 4 show the colors and magnitudes of the lens galaxies as compared to their neighbors and the predictions of spectrophotometric models.

Most of the lens galaxies for which we can accurately measure the colors have properties consistent with those of passively evolving early-type galaxies (KKF; Kochanek et al. 2000b). To interpret colors, we have used the solar metallicity, GISSEL96 version of the Bruzual & Charlot (1993, 2000, in preparation) spectrophotometric models. We assumed that galaxies begin forming stars at $z_f = 3$ ($H_0 = 65$ km s^{-1} Mpc^{-1}, $\Omega_0 = 0.3$, $\lambda_0 = 0.7$) with a Salpeter IMF for the early-type galaxies and a Scalo IMF for the late-type galaxies. For the early-type galaxies we use a "burst" model, in which star formation occurs at a constant rate for 1 Gyr and then ceases, and an "E/S0" model with an exponentially decaying star formation rate and a 1 Gyr e-folding timescale. For the late-type galaxies we used the star formation rate models for Sa, Sb, and Sc galaxies from Guiderdoni & Rocca-Volmerange (1988).

The lens galaxies are generally redder and brighter than their neighbors (see Fig. 3) and have colors consistent with early-type galaxies (see Figs. 3 and 4). In fact, most of the lenses for which we can measure the photometric properties lie on the passively evolving fundamental plane of early-type galaxies (see Kochanek et al. 2000b), and we can use this property to accurately estimate the unknown lens redshifts (average error $\langle \Delta z \rangle = -0.01 \pm 0.09$). Where the lens is undetected or the photometric models are too poor to test whether the lens lies on the fundamental plane, the faintness of the lens favors an early-type lens over a late-type lens because the higher M/L of early-type lenses makes them fainter for a given image separation (i.e., mass). In the rest B band the late-type, spiral lenses would be ~ 1.7 mag brighter for the same separation, based on the Faber-Jackson and Tully-Fisher relations (see Fukugita & Turner 1991; Kochanek 1996). For example, the spiral lens galaxy of the smallest separation lens, B0218+357 at $z_l = 0.68$, is brighter than many of the early-type lenses found in the wider separation systems. Only B0218+357 and PKS 1830−211 show evidence that they are late-type galaxies. They also contain molecular gas (e.g., Combes & Wiklind 1997; Carilli et al. 1998), and they show large differential and total extinctions of the lensed images (see Falco et al. 1999).

We now discuss particular characteristics of the individual lenses. In particular, we compare the goodness of fit for simple constant M/L models to those for isothermal dark matter lens models. We then add an external tidal field to the models and examine the improvement in the fit and the

---

[9] Allowing the photometric parameters to vary independently, constrained with their standard errors from Table 3, does not lead to significantly reduced model χ^2-values. However, the resulting parameters can be grossly inconsistent with the observed properties of the galaxy because of strong correlations between the photometric parameters.
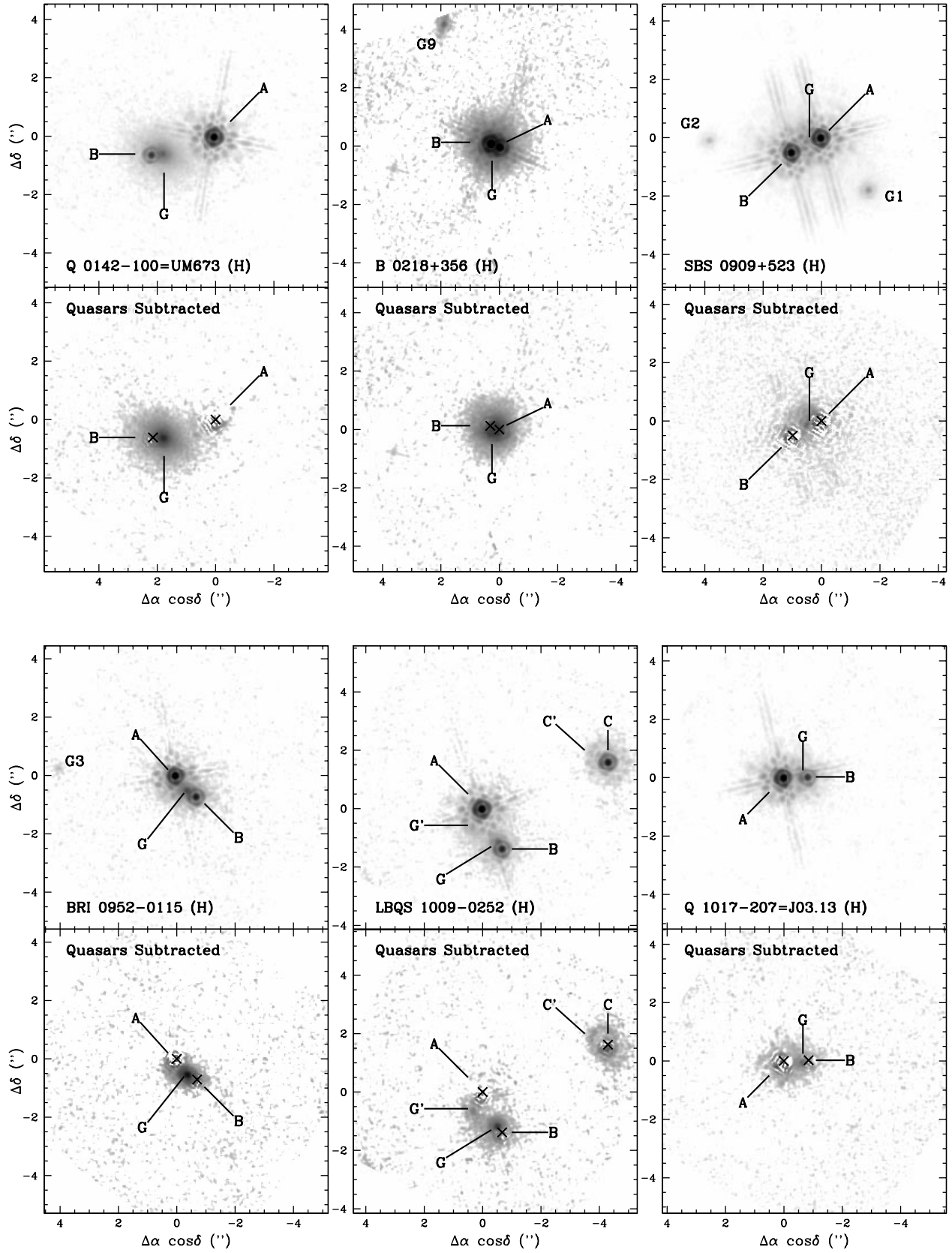
FIG. 1.—*HST* images of the 10 lens systems, with the filter indicated. Top panels show the final image of the system, with components labeled as in Tables 3 and 5. Bottom panels show the residuals after subtracting the quasars, with crosses marking the location of the quasar images.
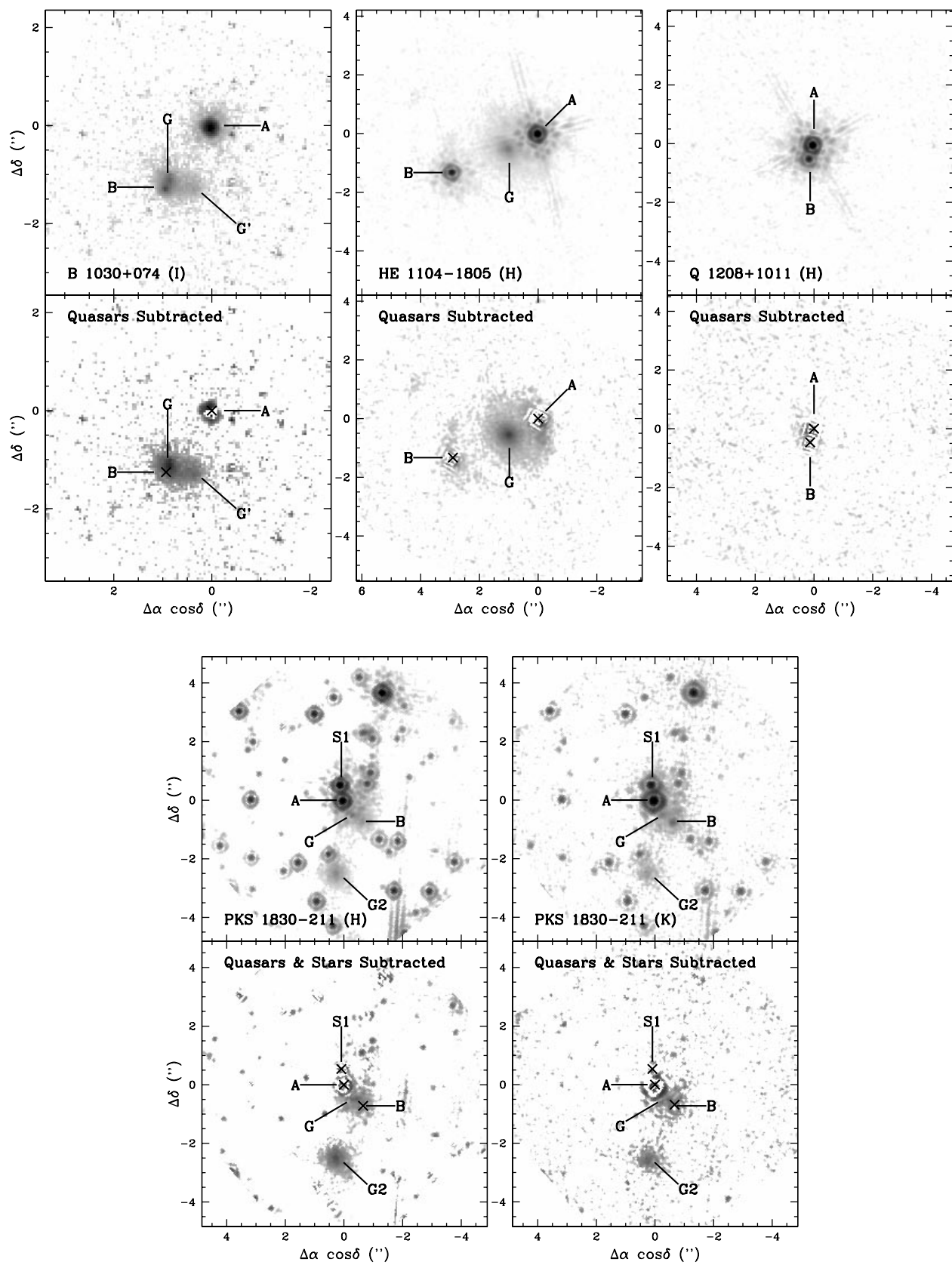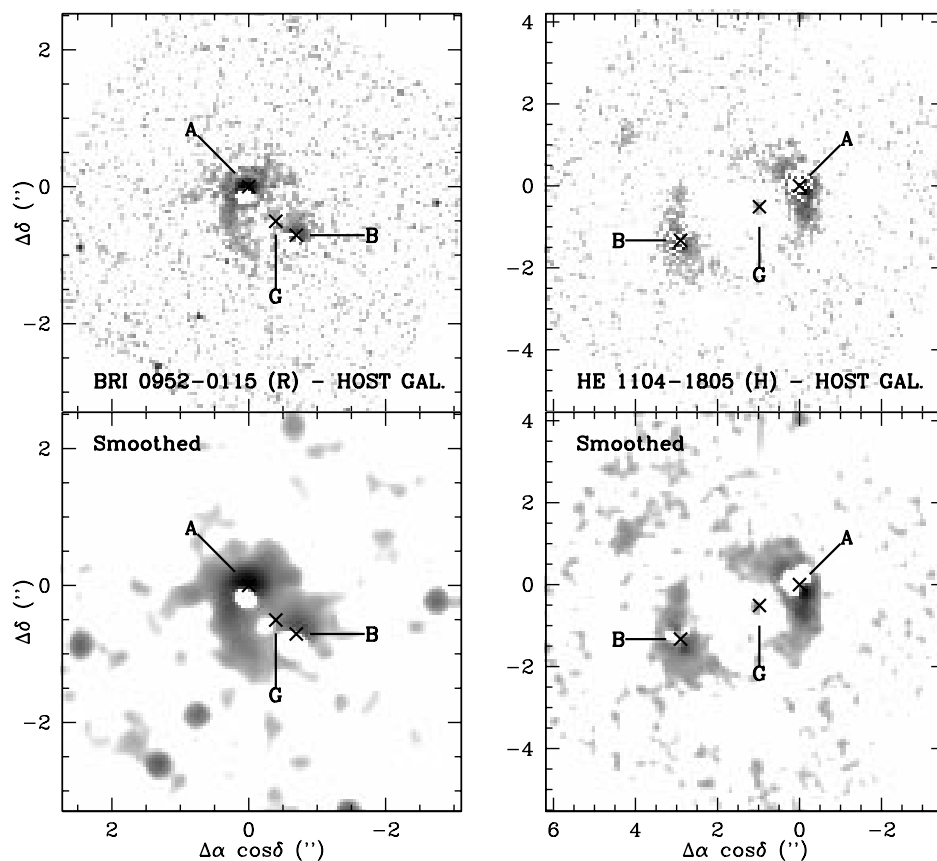
FIG. 1.—*Continued*

FIG. 2.—Quasar host galaxies we detected in BRI 0952−0115 (*left*) and HE 1104−1805 (*right*). The top panels show the images after subtracting both the quasar images and the lens galaxy, and the bottom panels show the same image after smoothing with a 2 pixel FWHM Gaussian filter.

relationship of the modeled external tide to our estimates from the lens environments. For all model classes we consider the predicted time delays, and their uncertainty ranges, for use in determinations of the Hubble constant. The level of detail possible for each object depends strongly on the data, geometry, and complexity of the individual systems.

5.1. Q0142−100 = UM 673

The $z_s = 2.72$ quasar Q0142−100 (UM 673) was discovered by MacAlpine & Feldman (1982) and found to be a $\Delta\theta = 2\farcs2$ lens by Surdej et al. (1987, 1988). Surdej et al. (1988) also identified the lens galaxy with a $z_l = 0.49$ Ca II absorption system with $R \simeq 19$ mag. A later spectrum (W. L. W. Sargent & M. Rauch 1998, private communication) showed three Mg II absorption systems located at $z_a = 0.43, 0.49$, and 0.56 (the strongest feature). Based on the WFPC2 V and R images, KKF found that the lens galaxy is well fitted by a de Vaucouleurs profile, and its colors match those of a passively evolving early-type galaxy at $z_l \approx 0.5$ (see Figs. 3 and 4).

A constant mass-to-light ratio lens model, with both the profile and ellipticity matched to the photometric models, provides a poor fit to the image positions and magnifications, with $\chi^2 \sim 80$. As also found by KKF, the SIE model must be significantly misaligned relative to the light to obtain a good fit—either the dark matter halo is itself misaligned, or external objects are exerting a strong tidal shear. The predicted time delays differ considerably between the two models, so a delay measurement and an estimate of H_0 could be used to discriminate between them.

Either model can be aligned with the lens and have an acceptable χ^2 with the addition of an external shear of $\gamma \sim 0.07$, but the strength and orientation of the shear show no correlation with shear estimates for the nearby galaxies. Since the cosmic shear estimate is comparable to that for the nearby galaxies, we should not expect such a correlation.

5.2. B0218+357

B0218+357 (Patnaik et al. 1993) includes two images of a compact, flat-spectrum radio core, offset from an Einstein ring image of the associated radio jet. The source redshift is $z_s = 0.96$ (Lawrence 1996). The lens redshift of $z_l = 0.685$ (Browne et al. 1993) was confirmed by the detection of H I (Carilli & Rupen 1993), CO, and other molecules (Wiklind & Combes 1995; Gerin et al. 1997; Combes & Wiklind 1997) in the lens galaxy. Grundahl & Hjorth (1995) detected the lens galaxy in the optical but could not characterize its properties. B0218+357 is of particular interest because it has a measured time delay of 10.5 ± 0.4 days (Biggs et al. 1999).

We simultaneously fit the H image with 2 point sources and an exponential disk galaxy. The estimated B−A quasar separation of (0\farcs307, 0\farcs126) matches the separation of the B1−A1 VLBI peaks (0\farcs3092, 0\farcs1274) to an accuracy of 2 mas. We detect the lens galaxy in all three bands and find that it is closer to the bright optical/faint radio core B, as expected from the radio flux ratio of the images. We quote our final results in Table 3 for a circular galaxy, because our fits could not distinguish the effects of a nonzero ellipticity. The lens galaxy is better fitted by an exponential disk than

TABLE 5
Lens Models

Lens	Model	x (arcsec East)	y (arcsec North)	b (arcsec)	R_e (arcsec)	ϵ $(1-b/a)$	θ_e	γ (Shear)	θ_γ	$h\Delta t$	χ^2/N_{dof}
Q0142−100........	SIE	1.764 ± 0.003	−0.574 ± 0.003	1.149 ± 0.004	...	0.27 ± 0.02	84 ± 2	...	...	80.1 ± 0.3	0/0
	SIE + γ	1.764 ± 0.003	−0.574 ± 0.003	1.195↔1.215	...	0↔0.27	≡61	0.069↔0.089	81↔118	84↔87	0/−1
	M/L	1.767	−0.552	3.27	≡0.59	≡0.25	≡61	...	...	121.3	75/2
	M/L+γ	1.764 ± 0.003	−0.574 ± 0.003	3.12 ± 0.07	≡0.59	≡0.25	≡61	0.07 ± 0.02	37 ± 6	115 ± 3	0/0
B0218+357	SIE	0.18 ± 0.02	0.08 ± 0.01	0.170 ± 0.001	...	0.10 ± 0.04	73 ± 6	...	...	2 ± 2	0.2/3
	SIE′	0.27 ± 0.01	0.118 ± 0.004	0.15 ± 0.01	...	0.4 ± 0.1	−36 ± 7	...	...	8.0 ± 0.7	1.5/3
SBS 0909+523......	SIE	0.4 ± 0.1	0.0 ± 0.1	0.5 ± 0.1	...	0.3 ± 0.4	56 ± 15	...	...	−34 ± 27	0/0
BRI 0952−0115.....	SIE	−0.396 ± 0.003	−0.506 ± 0.003	0.513 ± 0.002	...	0.183 ± 0.008	66 ± 1	...	...	5.2 ± 0.1	0/0
	SIE + γ	−0.396 ± 0.003	−0.506 ± 0.003	0.475↔0.527	...	0.00↔0.38	≡59	0.016↔0.1	66↔144	4.8↔5.3	0/−1
	M/L	−0.406	−0.483	3.63	≡0.14	≡0.47	≡59	...	...	8.5	109/2
	M/L+γ	−0.396 ± 0.003	−0.506 ± 0.003	3.49 ± 0.04	≡0.14	≡0.47	≡59	0.065 ± 0.008	−69 ± 3	8.7 ± 0.1	0/0
LBQS 1009−0252...	SIE	−0.537 ± 0.003	−1.097 ± 0.003	0.757 ± 0.006	...	0.08 ± 0.04	−58 ± 5	...	...	76.8 ± 0.5	0/0
Q1017−207..........	SIE	−0.66 ± 0.02	0.02 ± 0.02	0.438 ± 0.002	...	0.22 ± 0.03	−85 ± 11	...	...	18 ± 1	0/0
B1030+071	SIE + SIS	0.84 ± 0.01	−1.09 ± 0.01	0.587 ± 0.004	...	0.46 ± 0.06	−38 ± 4	...	...	63 ± 1	0/0
		0.35 ± 0.02	−1.23 ± 0.02	0.289 ± 0.002	...	≡0.00	...	...	...		
	M/L	0.83	−1.09	1.91	≡0.48	≡0.22	≡28	...	...	108	0.7/2
		0.35	−1.23	0.94	≡0.11	≡0.00	...	...	...		
	M/L+γ	0.84 ± 0.01	−1.09 ± 0.01	2.0 ± 0.3	≡0.48	≡0.22	≡28	0.1 ± 0.1	Any	114 ± 14	0/0
		0.35 ± 0.02	−1.23 ± 0.02	0.99 ± 0.1	≡0.11	≡0.00	...	...	...		
HE 1104−1805	SIE	0.974 ± 0.004	−0.510 ± 0.004	1.451 ± 0.005	...	0.341 ± 0.007	22.3 ± 0.2	...	...	−148 ± 1	0/0
	SIE + γ	0.974 ± 0.004	−0.510 ± 0.004	1.39↔1.40	...	0↔0.27	≡63	0.125↔0.142	2↔22	−129↔−131	0/−1
	M/L	1.004	−0.356	5.80	≡0.73	≡0.23	≡63	...	...	−263	2069/2
	M/L+γ	0.974 ± 0.004	−0.510 ± 0.004	4.65 ± 0.03	≡0.73	≡0.23	≡63	0.211 ± 0.004	17.6 ± 0.2	−192 ± 1	0/0
Q1208+1011........	SIS	0.105 ± 0.002	−0.381 ± 0.005	0.239 ± 0.001	...	≡0	...	...	...	9.4 ± 0.4	0/0
PKS 1830−211	SIE	−0.50 ± 0.08	−0.45 ± 0.08	0.48 ± 0.03	...	0.2 ± 0.2	−20 ± 22	...	...	19 ± 9	0/0
	SIS + SIS	−0.50 ± 0.07	−0.43 ± 0.03	0.45 ± 0.02	...	≡0	...	...	...	$16.3^{+0.2}_{-3.7}$	0/1
		−0.24 ± 0.02	−2.48 ± 0.02	0.3 ± 0.2	...	≡0	...	...	...		

Notes.—The models are (1) SIE is a singular isothermal ellipsoid; (2) SIE + γ is a SIE in an external field; (3) M/L is a constant mass-to-light ratio model matched to the photometric model for the lens galaxy in Table 3; and (4) $M/L + \gamma$ is a constant mass-to-light ratio model in an external tidal field. The model parameters are the lens position (x and y) in the same coordinates as were used for the photometric models in Table 3. The main lens galaxy is described by the critical radius parameter b as defined in eqs. (1)–(3), the major axis effective radius R_e (tied to the photometric models in Table 2), the ellipticity $1 - b/a$ (where b/a is the minor to major axis ratio) and the major axis position angle (PA) of the primary lens, and the amplitude (γ) of the external shear field and position angle (θ_γ) of the external shear field. The time delay $h\Delta t$ is given in days for $H_0 = 100\ h$ km s^{-1} Mpc^{-1} relative to the A(mag)Table 2 and an $\Omega_0 = 1$ cosmology. The final column gives the value of the χ^2 statistic for the fit and the number of degrees of freedom (N_{dof}) in the model. For the underconstrained SIE + γ models, we fixed the major axis orientation to that of the light, restricted γ to less than twice the external shear (γ_T or γ_{LSS}, Table 4), calculated a grid over the lens shape parameters, and determined $\Delta\chi^2 < 1$ ranges (min↔max). For B0218, the SIE′ model is identical to the SIE model, except that the lens position has been constrained to the center of the radio ring.
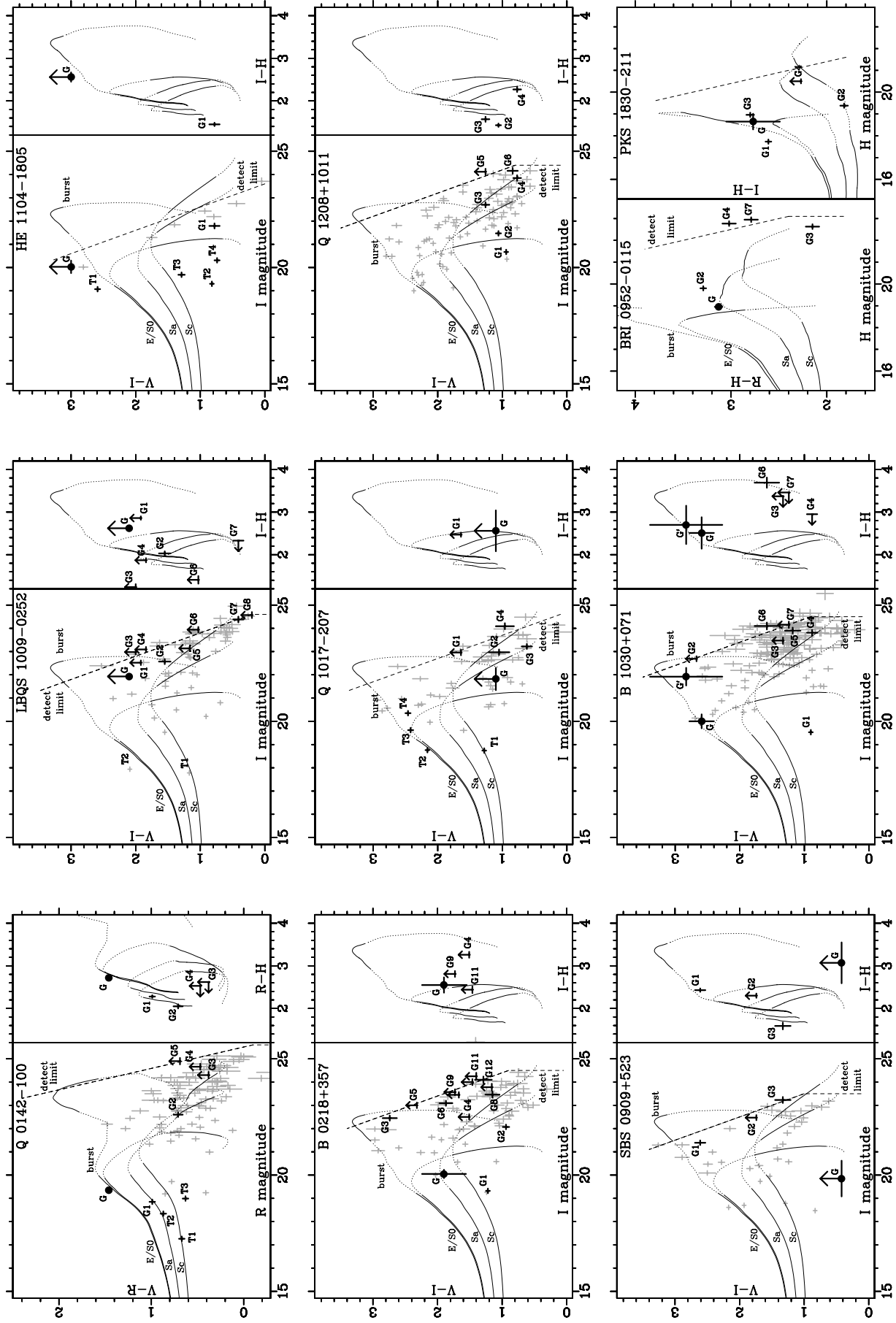
Fig. 3.—Colors and total magnitudes for the lens galaxies and their neighbors. Galaxies outside a radius of 20″ are shown in gray. SExtractor total magnitudes are offset-corrected (see § 2). The curves show photometric evolution models for L_* galaxies, alternating between solid and dotted lines at intervals of $\Delta z = 0.5$. Galaxies with $L < L_*$ should lie on the color-color curve which corresponds to their morphology type but will be shifted to the right in color-magnitude plots.
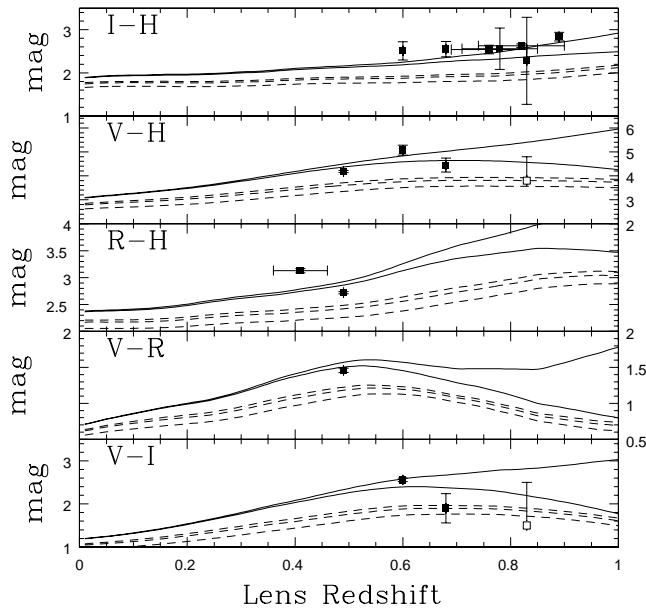
FIG. 4.—Lens galaxy colors. The curves (*from top to bottom*) show the burst, E/S0, Sa, Sb, and Sc evolution models. The solid points show the measured colors, and the open points show lower limits. The redshift error bars are the formal uncertainties in the fundamental plane/photometric redshifts estimated by Kochanek et al. (1999).

with a less luminous elliptical. The discrepancies could be explained either by a red bulge dominating the IR luminosity, or contamination of the colors due to the systematic errors in fitting this highly blended system. The NIC2 image has a galaxy position of $(0\overset{''}{.}178, 0\overset{''}{.}046)$ relative to A; the 25 mas positional uncertainty is dominated by the variations in the position found using different PSF models.

As a check of our NIC2 results, we also reduced and fitted the archival NICMOS/NIC1 image of the B0218+357 system (Jackson, Xanthopoulos, & Browne 2000). The undithered NIC1 image has the advantage of significantly smaller pixels and the disadvantages of a higher background noise level and poorer flattening. While the NIC1 and NIC2 quasar separations $(0\overset{''}{.}305, 0\overset{''}{.}126)$ agree within 2 mas, the NIC2 measurement is closer to the VLBI separation. The NIC1 lens position, $(0\overset{''}{.}184, 0\overset{''}{.}092)$ relative to A, is 46 mas away from the NIC2 value (see Fig. 5). Both the NIC1 and NIC2 images yielded markedly worse residuals when we used the lens galaxy position from one image to fit the other. We are forced to conclude that the existing data are unable to determine the position of G accurately. We adopt the mean of the NIC1 and NIC2 positions for the lens position, and one-half their difference as its uncertainty (~ 30 mas; see Table 3 and Fig. 5).

We used both NICMOS and VLBI constraints to fit lens models. The A/B VLBI images of B0218+357 each consist of 2 subimages called A1/A2 and B1/B2, with a separation within each pair of ~ 1 mas. The subimage separation vectors are roughly equal and radial, suggesting that successful lens models require nearly flat rotation curves to avoid large differences in the radial magnification at the two images. Following Patnaik, Porcas, & Browne (1995) we identified the VLBI components A1 and B1 with the A and B quasar images. Note, however, that an error in identifica-
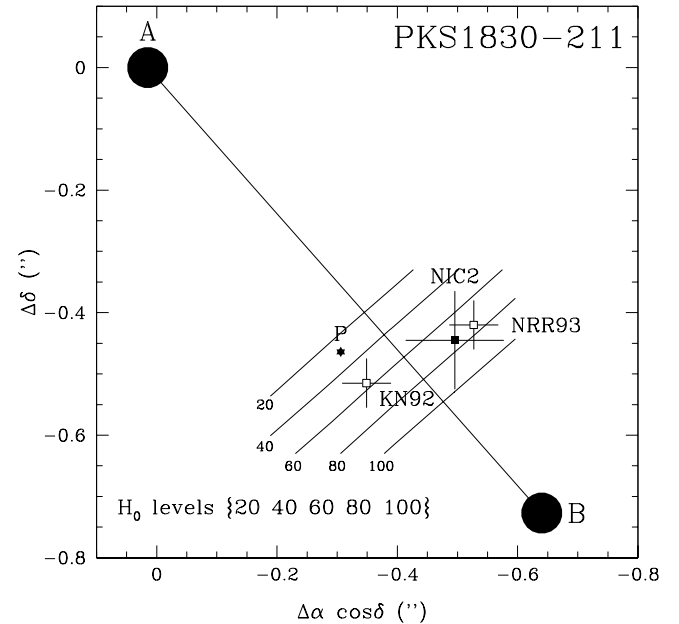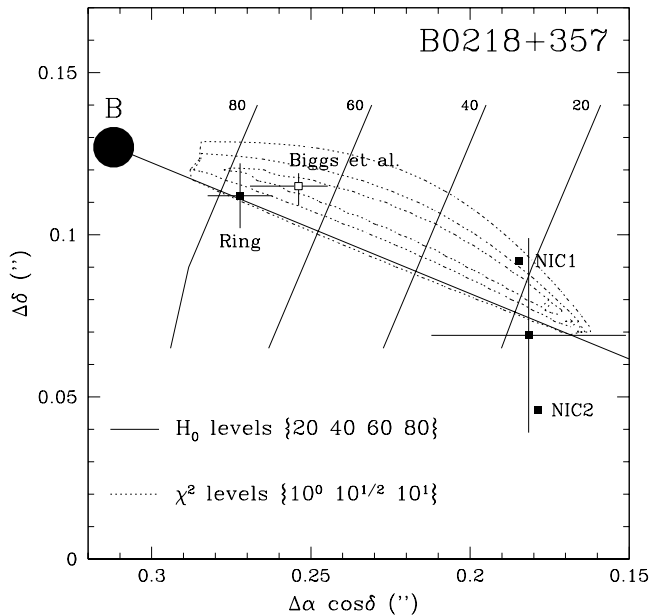
by a de Vaucouleurs lens, but the lens colors are not consistent with a single spectrophotometric model—the $V-I$ color is consistent with an $L \sim L_*$ spiral galaxy at the observed redshift, while the $I-H$ color is more consistent

FIG. 5.—Variation of H_0 with lens galaxy position in B0218+357 (*left*) and PKS 1830−211 (*right*). The solid contours show the variation in H_0 with the position of the lens given the measured time delays. For B0218+357 the positions derived from the NICMOS observations are the filled points labeled NIC1 and NIC2, and the point at their mean position with the large error bars is the lens position we used in our basic models. The point labeled " Ring " marks the estimated center of the Einstein ring (Patnaik et al. 1993). Using no direct constraints on the lens position, Biggs et al. (1999) found the position marked by the open point from their lens models. Using the same constraints, we find a much broader degeneracy in the models for the lens position, illustrated with the dashed χ^2 contours. The filled points for PKS 1830−211 mark the positions of the lens galaxy (labeled NIC2) and the pointlike source P. The open points give the lens positions found in the models of Kochanek & Narayan (1992, labeled KN92) and Nair et al. (1993, labeled NRR93).

tion would have negligible effects on the models because of the very small pair separations. We modeled B0218+357 using the A1–B1 and A2–B2 VLBI image pairs and magnifications (Patnaik et al. 1995) combined with our position for the lens galaxy relative to the A1–B1 pair. We assumed that the VLBI positions of the components were accurate to 0.1 mas and used the Patnaik et al. (1995) flux density uncertainties.

We fit only the SIE model to the system. When the lens position is constrained by the NICMOS results (model SIE in Table 5), we obtain an extraordinarily low estimate for the Hubble constant, $H_0 = (20 \pm 20)(\Delta t/10.5 \text{ days})$, given the Biggs et al. (1999) time delay. The low delay is entirely a consequence of the lens position, as we show in Figure 5. Using no constraints Biggs et al. (1999) derived a lens position of $(0\farcs252 \pm 0\farcs012, 0\farcs115 \pm 0\farcs005)$, but they appear to have underestimated the full extent of the degenerate region. When we remove the lens position constraints, keeping all other constraints the same, the χ^2 contours have a degenerate region parallel to the A–B quasar separation. The estimated Hubble constant rises monotonically as the lens approaches image B. An alternative constraint on the lens center comes from the centroid of the radio ring (at $0\farcs27 \pm 0\farcs01, 0\farcs11 \pm 0\farcs01$; Patnaik et al. 1993), although the systematic errors in such a centroid are of order $2\epsilon_\phi b \gtrsim 0\farcs03$, where ϵ_ϕ is the ellipticity of the lens potential and b is the critical radius.

In model SIE′ we constrain the lens center to the location of the ring centroid. To first order, the ring centroid defines the position of the background source, which should be close to the lens. The fit has $\chi^2 = 1.5$ and gives a larger Hubble constant, $H_0 = 76 \pm 7$, but it requires a large ellipticity for the lens ($\epsilon = 1 - b/a = 0.4 \pm 0.1$). The luminous galaxy is not this flat (see Fig. 1), and the tidal shear is negligible. Thus, it is likely that both the NICMOS and ring centroid estimates of the lens position are systematically incorrect. It is important to obtain an accurate direct measurement of the lens position.

Other changes to the lens models appear relatively unimportant. We experimented with changing the lens potential by using a pseudo-Jaffe model and varying the break radius a.[10] When the break radius becomes smaller than the ring radius, the χ^2 of the fit begins to rise along with the Hubble constant estimate. But the rise in H_0 is insignificant unless the χ^2 of the fit is so large that the model must be rejected.

Of all 10 lenses, B0218+357 is the most isolated in the sense that the estimated tidal shear at the location of the lens is only $\gamma_T \sim 1\%$. This is in marked contrast to the other systems with measured time delays, Q0957+561 (Schild & Thomson 1995; Kundić et al. 1997), PG 1115+080 (Schechter et al. 1997), B1608+656 (Fassnacht 1997), and PKS 1830−211 (Lovell et al. 1998), which are all embedded in small groups or clusters of galaxies. The morphology-density relationship (e.g., Dressler 1980) suggests that late-type galaxies are more likely to be isolated; and of the six lenses with time delays, only B0218+357 and PKS 1830−211 are late-type galaxies. The low source red-

shift means that the large-scale structure shear of $\gamma_{\text{LSS}} \simeq 0.02$ is also small.

5.3. SBS 0909+532

SBS 0909+532 was discovered by Kochanek et al. (1997) as two images of a $z_s = 1.377$ quasar separated by $1\farcs11$. These redshifts were confirmed by Oscoz et al. (1997). With the NICMOS observations we have discovered a large, bright galaxy between the quasar images, confirming that SBS 0909+532 is a gravitational lens. The lens redshift is now measured to be $z_l = 0.83$ (Lubin et al. 2000). A significant residual corresponding to the core of the lens is also found in the WFPC2 I band image after subtracting the two quasars, but the lens is undetected in the WFPC2 V band image. The lens galaxy has a large effective radius, with a correspondingly low surface brightness. The colors of the lens are poorly measured but consistent with those of an early-type galaxy at the observed redshift. The lens is in a typical tidal environment, with $\gamma_T \simeq 0.05$ and $\gamma_{\text{LSS}} \simeq 0.03$.

5.4. BRI 0952−0115

BRI 0952−0115 was discovered by McMahon, Irwin, & Hazard (1992) as a pair of $z_s = 4.5$ quasars separated by $0\farcs9$. From WFPC2 imaging and photometry, KKF found that the lens galaxy was an $R \simeq 22$ mag, flattened early-type galaxy.

The lens appears to be a typical early-type lens galaxy, with a fundamental plane redshift estimate of $z_{\text{FP}} = 0.41 \pm 0.05$ (Kochanek et al. 2000b). A constant M/L lens model fails to fit the lens constraints ($\chi^2 = 109$), but a modest external shear in a $M/L + \gamma$ model yields a good fit. We expect no correlations of the shear with the local environment because the local estimate of $\gamma_T \simeq 0.03$ is significantly smaller than $\gamma_{\text{LSS}} \simeq 0.05$. Moreover, galaxy G3, which dominates the local shear estimate, is likely to be a late-type galaxy (it is unusually blue in $R - H$), so we have probably overestimated its tidal effects. While we cannot differentiate between SIE and M/L models based on the image constraints, the time delays depend strongly on the amount of dark matter in the lens.

After subtracting the quasars and the lens, the residual R-band image reveals a prominent arc, extending asymmetrically from quasar image A (see Fig. 2). Its shape matches the shape predicted for the lensed image of an extended source centered on the quasar, suggesting that it is part of an Einstein ring image formed from the $z_s = 4.5$ quasar host. The H-band image hints at similar but significantly fainter residuals. The limiting magnitudes of the observations in $\simeq 0\farcs2$ square boxes (4 PC pixels or 5 subsampled NICMOS pixels) are approximately 24.9 and 22.8 mag arcsec^{-2} in R and H, respectively. The brightest part of the ring, which is well separated from the quasar, has a mean surface brightness of 22.4 mag arcsec^{-2} in R. All of our spectrophotometric models for formation redshifts of $z_f \approx 5$–10 predict $R - H$ colors in the range 1.0 to 1.5 in the absence of extinction. Therefore, for a stellar population we would expect the H surface brightness of the arc to be approximately 20.4 mag arcsec^{-2}, which should easily have been detected in our H band image. The R filter is almost exactly centered on the Lyα line of the quasar, so the extended emission could be dominated by line emission similar to the Lyα emission regions seen near MG 2016+112 (Schneider et al. 1986). Such emission regions are rare (a modest amount of dust will quench the

---

[10] The pseudo-Jaffe model is the difference of two SIE models (eq. [1]) with scale lengths of 0 and a, respectively. It corresponds to a three-dimensional density distribution with $\rho \propto 1/[r^2(r^2 + a^2)]$ similar to the Jaffe (1983) model with $\rho \propto 1/[r^2(r + a)^2]$. When the break radius a is large compared to the ring radius the model acts like an SIE, but by reducing a we model a more compact, finite mass distribution (see Keeton & Kochanek 1998).

Lyα emission) and surveys for high-redshift galaxies based on detecting high equivalent width Lyα emission have been mostly unsuccessful (e.g., Thompson, Djorgovski, & Trauger 1995). Thus, the origin of the lensed host light remains unclear.

5.5. *LBQS 1009−0252*

LBQS 1009−0252 (Hewett et al. 1994; Surdej et al. 1994) consists of two $z_s = 2.74$ quasars, A and B, separated by $1\farcs53$. A third quasar, C, at a redshift of $z_C = 1.62$ lies only $4\farcs6$ to the northwest of the lens. No lens galaxy had been detected prior to our observations, although a strong Mg II absorption line system at $z = 0.869$ has been proposed for the lens redshift.

We clearly detect the lens galaxy near quasar B in the *H*- and *I*-band images. A de Vaucouleurs profile fits the lens with an effective radius of $\approx 0\farcs2$, but there was insufficient flux to determine its ellipticity. The galaxy is not detected in the shorter *V*-band observation. The fundamental plane lens redshift estimate, $z_{FP} \approx 0.8 \pm 0.1$ (Kochanek et al. 2000b), agrees well with the Mg II absorption redshift. In the *H*-band image we find a residual component G′ near quasar A and an extended residual, C′, around quasar C. G′ might be the lensed quasar host or a fainter companion to the lens galaxy, and C′ is presumably the host galaxy to quasar C. G′ and C′ are not detected in the optical images.

We estimate that the quasar host galaxy C′ can produce an effective shear of $\simeq 0.08$ at the lens after correcting for the redshift differences. This is comparable to the estimated shear generated by the other galaxies, but in an orthogonal direction. Given the uncertainties in our estimate, either C′ or the other neighbors could dominate the external shear. While we fit only an SIE lens model, the derived major axis of the SIE model is consistent with an external shear dominated by C′. Thus, C′ may be an extreme example of the "large-scale structure" shear contribution being associated with a detectable object that we would include in our estimate of the local shear environment in the absence of redshift information. The surprisingly blue $I−H$ color for G3 is not due to SExtractor errors, it is simply much fainter in the *H*-band image than its neighbor G4.

5.6. *Q1017−207 = J03.13 = CTQ 286*

Q1017−207 (Claeskens, Surdej, & Remy 1996) was confirmed by Surdej et al. (1997) to be a pair of $z_s = 2.545$ quasars separated by $0\farcs85$. Remy et al. (1998) obtained WFPC2 *V*- and *I*-band images, in which they found no sign of a lens galaxy.

The lens galaxy is clearly detected in our NICMOS *H*-band image. Because the unfavorable contrast precludes a well-constrained fit to the lens galaxy, we fit a round de Vaucouleurs model with scale length of $0\farcs3$. Using the astrometric and structural properties from the *H* image we can estimate the luminosity of the galaxy in the *I* band, because the core of the galaxy is seen in the *I* image at the same location as in the *H* band after subtracting the quasar images. The *V*-band image yielded only an upper limit. The $I−H$ color of 2.56 ± 0.48 mag is consistent with an early-type galaxy at $z_{FP} = 0.78 \pm 0.07$ (Kochanek et al. 2000b). We fit only the SIE model, finding good fits with a moderately elliptical galaxy having an east-west orientation for the major axis. However, the external shear estimates (including the expected cosmological shear) for the field

suffice to allow significant freedom to the true orientation of the lens.

5.7. *B1030+074*

B1030+074 was discovered by Xanthopoulos et al. (1998) as a pair of flat-spectrum radio sources, A and B, separated by $1\farcs56$. Both radio sources had optical quasar counterparts in WFPC2 *V* and *I* images. They noted that the lens consists of two components G and G′. This is confirmed by their later NIC1 image. We include this lens in our discussion because its general morphology and *HST* observations match our CASTLES subsample, and because the VLBI data provide a useful absolute astrometry check on our procedures.

We measured the B–A separation between the two quasars on the WFPC2 *I* image to be $(0\farcs928 \pm 0\farcs003, -1\farcs257 \pm 0\farcs003)$, in agreement with the VLBI offset of $(0\farcs934 \pm 0\farcs001, -1\farcs258 \pm 0\farcs001)$ from Xanthopoulos et al. (1998) to within 6 mas, for a joint $\chi^2/N_{dof} = 3.6/2$. We could not obtain better results from the NIC1 data because the combination of chip defects, chip edges, cosmic-ray persistence, and the lack of dithering leads to a very poor image. We find that G is well fitted by a de Vaucouleurs profile and that it has the color, flux, and scale length expected for a red, early-type galaxy at redshift 0.60. Although the color of G′ is nearly the same as that of G, it is better fitted by an exponential disk profile. The two-component photometric model fits the image well, and we conclude that G and G′ are distinct galaxies.

For the lens models, we used as position constraints our NICMOS galaxy position and the Xanthopoulos et al. (1998) VLBI image radio positions (with an assumed error of 2 mas). We used an image flux ratio of $A/B = 15 \pm 6$ based on the average radio flux ratio, and we used an error equal to twice the dispersion in the flux ratio. We used two-component lens mass models to represent B1030+074. To reduce the number of free parameters in the dark matter model, we allowed only galaxy G to be an elliptical SIE, while G′ was modeled as a circular SIS with a critical radius scaled to that of G by the square root of their luminosities. Without an external shear, the orientation of the SIE models is inconsistent with that of the light. The constant M/L lens model, however, which included an elliptical de Vaucouleurs lens for G and a circular exponential lens for G′ with masses scaled to their relative brightnesses, provided a good fit to the lens constraints, with $\chi^2/N_{dof} = 0.7/2$. This is the only case in our sample where a constant M/L model can fit the constraints in the absence of an external perturbation.

B1030+074 is one of the two systems where the local shear $\gamma_T \simeq 0.11$ estimated from the nearby galaxies is significantly larger than the large-scale structure contribution $\gamma_{LSS} \simeq 0.03$, and we might hope to find a strong correlation between the shear required by the lens model and the predictions from the environment. Unfortunately, the galaxy dominating the local shear estimate, G1, is too blue ($V − I = 0.9$ mag) to be a early-type galaxy at the lens redshift ($V − I \simeq 1.7$ mag), which means that we have overestimated its shear contribution and cannot make firm statements about the environment.

5.8. *HE 1104−1805*

HE 1104−1805 was discovered by Wisotzki et al. (1993, 1995) as two $z_s = 2.319$ quasars separated by $3\farcs19$. Courbin,

Lidman, & Magain (1998b) detected the lens galaxy in ground-based observations, with estimated magnitudes of $J = 19.0 \pm 0.2$ and $K = 17.1 \pm 0.2$. Remy et al. (1998) detected the lens galaxy in their WFPC2 I images but not their V images and suggested that it was an early-type galaxy at $z_l = 1.32$, where the quasar spectrum has a metal absorption feature. Since all quasars show an average of one metal line absorption system per unit redshift down to a rest equivalent width of around 1 Å (Steidel 1990), independent of whether or not they are lensed, there is no convincing reason to adopt the redshift advocated by Remy et al. (1998).[11]

The lens galaxy's colors are consistent with a high-redshift early-type galaxy, and we estimate its redshift is $z_{FP} = 0.77 \pm 0.07$ based on the fundamental plane (Kochanek et al. 2000b). HE 1104−1805 is very unusual in that the lens is near the bright image, rather than the faint one. Simple models can match this configuration only for a narrow range of parameters which imply a large misalignment between the light and simple ellipsoidal lens models. The mass can be aligned with the light only if the shear field is twice as strong as estimated in Table 4. The image separation of 3″2 is also much larger than that of a typical lens (the median is 1″5), suggesting that the separation is boosted by the presence of a group or cluster, although none is obviously present in the WFPC2 fields. The narrow parameter range is a consequence of the peculiar flux ratio, which may be distorted by either intrinsic source variability or microlensing (see Wisotzki et al. 1995). Although we can find less extreme lens models if we drop the flux ratio as a constraint, the required change in the flux ratio (a factor of 4) is inconsistent with the structure of the host galaxy (see below), where the A image is clearly more magnified than the B image.

In the residuals of the H image we clearly see two arc images of the quasar host galaxy. We fitted a circular exponential host galaxy model, lensed by the SIE + γ model, and derived an intrinsic host galaxy magnitude of $H = 21.1$, corresponding to $\sim 0.3 L_*$ for a burst population evolution model. Fitting a de Vaucouleurs model gives $H = 20.5$ mag, with slightly larger residuals. The corrections to the magnitudes of the quasar nuclei are less than 0.1% as a result of the additional host component. By scaling and adding the H image of the arcs to the I and V images, we estimate that the arc has $I - H > 3$ mag and $V - H > 2.5$ mag. This is significantly redder than all but the burst spectrophotometric models. The E/S0 and Sabc models all have $I - H \simeq 2.4 \pm 0.4$ mag for formation redshifts of $3 \lesssim z_f \lesssim 15$, while the burst models have $I - H \simeq 3.5$ to 5.0 mag. Thus, the host galaxy either has little ongoing star formation or is dusty.

5.9. Q1208+1011

Q1208+1011 was discovered by Maoz et al. (1992) and Magain et al. (1992) as two images of a $z_s = 3.8$ quasar separated by 0″45. The indistinguishable redshifts were confirmed by Bahcall et al. (1992a). WFPC1 images (Bahcall et al. 1992b) yielded no evidence for a lens galaxy. Siemiginowska et al. (1998) estimated that an early-type lens galaxy would have $20 < H < 21$ mag for the most plausible lens

redshift range, while a late-type lens would be 0.5–1.0 mag brighter. The most plausible redshift range includes a $z_a = 1.13$ Mg II absorption system, and we use this redshift to compute lens model time delays.

We failed to detect the lens galaxy in either the NICMOS or the WFPC2 images. Our detection limit for an $r_e = 0″3$ de Vaucouleurs galaxy located exactly between the quasar images is approximately 20 H magnitudes, still consistent with the system being a normal gravitational lens where the lens galaxy is masked by the bright quasars. It is purely a problem of contrast, as the detection limit in the field away from the quasars is closer to 22 H magnitudes for the same galaxy. The detection limits for the lens galaxy at V and I are significantly worse. Without even a position for the lens we cannot explore models more complicated than a simple, circular SIS model.

5.10. PKS 1830−211

PKS 1830−211 was identified as a lens by Subrahmanyan et al. (1990), although the details became clear only with the higher resolution radio maps of Jauncey et al. (1991). It is an Einstein ring containing two bright images of the radio core with a separation of 0″971 $\pm$ 0″002 (Jones et al. 1993). The source is strongly variable and a time delay of 26 $\pm$ 5 days has been measured (Lovell et al. 1998). Molecular absorption has been detected at $z_l = 0.886$ (Wiklind & Combes 1996; Gerin et al. 1997; Carilli et al. 1998) largely in front of the B (southwest) image (Frye et al. 1999). Lovell et al. (1996) also found a $z_a = 0.19$ H I absorption feature. X-ray spectra also show a large amount of absorption due to dust and gas (Mathur & Nair 1997). Using infrared observations, the source components have been resolved (Courbin et al. 1998a; Frye et al. 1999), and the quasar redshift of $z_s = 2.507$ has been measured (Lidman et al. 1999).

We detect the bright quasar and the lens galaxy in I, H, and K, while the faint quasar is only detected unambiguously in the K band. The lens galaxy is best fitted by an exponential disk which is sufficiently round to make estimates of the PA unreliable. The astrometry for the lens galaxy is complicated by the presence of a feature, labeled P in Table 3, between the quasars and near the center of the lens galaxy. It appears to be pointlike, but its colors are redder than those of the nearby M star, and similar to those of the lens galaxy G (see Table 3). In the region we used for our fits there are 10 stars in an area corresponding to 36 Einstein ring areas, leading to an expectation of ~ 0.3 stars per ring area. Thus, the feature could be either the bulge of the lens galaxy or a superposed, red Galactic star. We decided to assume that the feature is a superposed Galactic star and to adjust the position of the lens and the feature separately.

The positional uncertainty for P is less than 6 mas. The corresponding uncertainty for G is much larger, ~ 80 mas, because of its low surface brightness and the proximity of A and P. The K-band image yields positions for the lensed compact images A and B with positional uncertainties less than 3 mas, as expected for bright pointlike sources. Courbin et al. (1998a) noted that their position for the SE component is likely to be contaminated by the lens galaxy. Indeed, while their location for the brighter NE component is consistent with our determination, their position for the SW component is shifted toward G, disagreeing with ours at the 3–4 σ level for their 0″05 standard errors. Our esti-

---

[11] See the discussion in Siemiginowska et al. (1998) on using metal line absorption features to estimate lens redshifts.

mated separation of $0\rlap{.}''973 \pm 0\rlap{.}''004$ is an excellent match to the mean VLBI separation of $0\rlap{.}''974 \pm 0\rlap{.}''002$ (Jones et al. 1993). The galaxy G is close to the lens model position of Nair, Narasimha, & Rao (1993), while the feature P is close to the lens model position of Kochanek & Narayan (1992). Figure 5 shows the locations of the various components as well as the lens positions in the two models.

For the lens models, we used the NICMOS lens position, combined with the more precise VLBI image positions and flux ratios. We do not use any constraints from the radio ring. Given the Lovell et al. (1998) time delay and an SIE model for G, we find a Hubble constant of $H_0 = (73 \pm 35)(\Delta t/26 \text{ days}) \text{ km s}^{-1} \text{ Mpc}^{-1}$. The uncertainties in H_0 from the lens model are dominated by the uncertainties in the lens position (see Fig. 5). The system can also be well fit using two SIS lenses (model SIS + SIS in Table 5), one located at the position of G and the other at the position of the close neighbor G2 (see below), and in these models the values of H_0 are reduced by approximately 15%.

We identified several other galaxies in the field, in particular the bright galaxy G2, only $2\rlap{.}''5$ to the south of the lens system. The lens galaxy, G, and the nearby galaxies G1 and G3 have similar colors ($I - H = 2.6$ to 2.8 mag), while the very close neighbor G2 is significantly bluer ($I - H = 1.8$ mag). Although the lens is better fitted by an exponential profile, its $I - H$ color is closer to that of an early-type galaxy than a late-type galaxy at $z_l = 0.9$. However, the high estimates (Courbin et al. 1998a; Falco et al. 1999) for the differential ($\Delta E_{B-V} \approx 3.0$ mag) and total extinction for the blue image ($E_{B-V} \approx 0.6$ mag) mean that the lens galaxy colors are significantly affected by extinction. The molecular absorption is almost certainly associated with the primary lens galaxy, and the similar colors of G1 and G3 suggest that they lie at the same redshift.

The relatively blue galaxy G2 is the only candidate for producing the H I absorption at $z_a = 0.19$ reported by Lovell et al. (1996). If it is a low-redshift galaxy, it is not an important contributor to the lens model. An L_* galaxy at $z = 0.2$ has $H_* = 15$–16 mag (early to late type) compared to $H_* = 18$–20 mag at $z = 0.9$. If G2 is at the lens redshift, it is an $\sim L_*$ galaxy producing strong tidal perturbations ($\gamma_T \simeq 0.08$), whereas if it is at the H I absorption redshift of 0.19 it is a $\sim 0.01 L_*$ dwarf galaxy contributing a negligible tidal shear ($\gamma_T \simeq 0.004$). A model consisting of two SIS lenses representing galaxies G and G2 fits the data well (model SIS + SIS in Table 5), and the critical radius ratio of $b_{G2}/b_{G1} = 0.7 \pm 0.4$ implies a luminosity difference of 0.5 ± 0.5 mag which is consistent with the H-band magnitude difference of 0.6 ± 0.6 mag. The uncertainties in the luminosity ratio are dominated by the uncertainties in the galaxy scale lengths. G2 also has the well-structured appearance of a massive galaxy and an H-band surface brightness similar to that of G, G1, and G3. We conclude that G2 lies at the redshift of G.

6. CONCLUSIONS

Because of the small angular scales of gravitational lenses, *HST* is essential for accurate surface photometry of gravitational lens galaxies. Furthermore, NICMOS allows us to observe lens galaxies where they emit most of their energy, rather than beyond the sharp spectral breaks that make them difficult to study in the optical. Here we outlined our survey procedures and present 10 double lenses where a combination of limited constraints and extreme contrast

between the lens and the source restricts our analysis to relatively simple models. For these 10 targets, we have made the first detections of a lens galaxy in three cases (SBS 0909 + 532, LBQS 1009 − 0252, and Q1017 − 207), and we were unable to detect the lens in only one case, Q1208 + 1011. Given our estimated detection limits, our failure to find the lens galaxy is still consistent with the lens hypothesis. We obtained quantitative surface photometry on six systems, Q0142 − 100, BRI 0952 − 0115, LBQS 1009 − 0252, Q1017 − 207, B1030 + 074, HE 1104 − 1805, and PKS 1830 − 211, and we clearly detected the host galaxy of the lensed quasar in BRI 0952 − 0115 and HE 1104 − 1805.

Most of the lens galaxies appear to be early-type galaxies based on their colors and luminosities, as previously noted by KKF and predicted in most theoretical models (Fukugita & Turner 1991; Kochanek 1994, 1996; Maoz & Rix 1993). Usually where we lack accurate photometry on the lens, an early-type galaxy is favored because the lower M/L of late-type galaxies should make them brighter than we actually observe. For example, the spiral lens galaxy in B0218 + 357 is quite luminous for a lens despite its being the smallest separation lens known. We have found (KKF; Kochanek et al. 2000b) that most of the doubles for which we obtained quantitative photometry (Q0142 − 100, BRI 0952 − 0115, LBQS 1009 − 0252, B1030 + 074, and HE 1104 − 1805) lie on the fundamental plane (Djorgovski & Davis 1987; Dressler et al. 1987). The two clear late-type lenses, B0218 + 357 and PKS 1830 − 211, also show large differential extinctions (see Falco et al. 1999) and contain molecular gas (e.g., Combes & Wiklind 1997; Carilli et al. 1998).

We fit a set of four standard lens models designed to explore the issues of dark matter and the lens environment. We used either a constant M/L lens model matched to our photometric fits or a singular isothermal ellipsoid. We fit each model in isolation and then with an external shear to represent perturbations to the model from nearby galaxies or potential perturbations along the ray path. Without external tidal perturbations, the constant M/L models usually could not fit the lens constraints, and the dark matter models could only fit the lens constraints if misaligned relative to the luminosity. With the addition of a modest external shear, either model could fit all the lenses because the two-image lenses provide so few constraints on the models. In general, the constant M/L and dark matter models predict very different time delays for the two-image lenses and are hence distinguishable.

We cataloged the galaxies found within $\sim 100 \; h^{-1}$ kpc of the lenses and estimated the local tidal environment based on the luminosities of the neighboring galaxies. If the galaxies have extended dark matter halos, they produce significant shears at the lens galaxy of $\gamma_T \sim 0.05$, while if they have a constant M/L, they produce a negligible perturbation of $\gamma_T < 0.01$. The dark matter estimates for the tidal shear are comparable to the shears necessary to find good lens models, but there is no clear correlation between the shear from the lens model and the estimate from the local environment. Part of the problem is that the shear perturbations created by large-scale structure along the ray path (see Bar-Kana 1996; Keeton et al. 1997) are of comparable strength to those from nearby galaxies. The poorly constrained two-image lenses are ill suited for quantitative studies of their tidal environments.

Two of these 10 lenses, B0218+357 (Biggs et al. 1999) and PKS 1830−211 (Lovell et al. 1998), have measured time delays. Unfortunately, the short exposures necessary for a survey project cannot measure the position of the lens galaxy in these two systems with sufficient precision to accurately determine the Hubble constant. We can measure the positions with an accuracy of 0″.03–0″.07, but we need the positions to an accuracy less than 0″.01. For PKS 1830−211 only longer observations are necessary— the data obtained here demonstrate that the uncertainties would be easily resolved given a higher signal-to-noise ratio. For B0218+357 the solution is less clear, because we are limited by the small component separations rather than the signal-to-noise. Better image sampling (currently obtainable only in the ultraviolet for *HST*) combined with concurrent PSF measurements might resolve the problem.

APPENDIX

NICMOS IMAGE REDUCTION

We developed the NICRED reduction package[12] for NICMOS data sets which are acquired in the MULTIACCUM mode (MacKenty et al. 1997), where the detector is read out nondestructively at intervals throughout the exposure. By recording all readouts, pixels that become saturated or are struck by cosmic rays during the exposure can still be used. The ability to avoid saturation is an enormous advantage for lens systems because of the extreme surface brightness contrast between the quasar images and the lens or host galaxies.

The first step in NICRED is to subtract the dark current and bias frame by frame from each MULTIACCUM subexposure. The library darks from the *HST* archive left unacceptably large dark-frame structures in the reduced images. Therefore, we constructed "sky dark" frames from our own images, which contained mainly empty sky: we masked pixels with significant detected flux in all our raw images, and median-combined the masked images to produce the sky dark image. A change in the flight software on 1997 August 21 altered the dark frame structure and forced us to construct two separate sky-darks. Among the data taken before 1997 August only two images (Q0142−100 and Q1634+267) had sufficient empty sky to build the sky-dark. Here we first combined the masked raw images separately for each target and then kept only the lowest of the two target signals in each pixel.

Following dark subtraction, we fit, for each pixel, a linear function to the run of counts as a function of exposure time at readout. We allow for the possibility of a cosmic-ray hit between readouts by fitting two line segments, with the same slope, before and after each readout. Thus, for a sequence with N readouts, we consider N trial intervals where a cosmic ray might have hit. For each trial, we derive the slope and two intercepts. If the difference between the two intercepts is large, compared with the residuals of the fit, a cosmic-ray hit is likely. Out of the N trials, we choose the trial with the largest difference-to-residual ratio r_{diff} as that where the hit occurred. If no trial has a statistically significant r_{diff}, no cosmic-ray hit has occurred, and we perform a traditional linear regression with a single intercept. The slope derived for each pixel represents its count rate.

We cannot apply a simple flat-field correction, because the NICMOS detectors suffer from the "pedestal effect" (Skinner 1997), a global shift in the signal level that affects each readout. In general, the shift is different for each readout but is the same for all quadrants of the NICMOS detector. As a consequence, the final image reflects the actual count rates plus some global constant. When the flat-field correction is made, the additive constant makes an incorrect contribution to the flat-field pattern, resulting in a poorly flattened image. Because our images are predominantly blank sky, we can correct for this problem by masking out the objects in each image and assuming that the rest of the image is a constant, multiplied by the flat, plus another constant for the pedestal effect. We simultaneously determine the two constants with a least squares fit and remove them with the appropriate flat-field correction.

Each of the individual readouts is affected by the pedestal effect, so the counts in the individual pixel fits are not a linear function of exposure time, and the cosmic-ray rejection algorithm can fail. We use an iterative scheme to correct for this nonlinearity. For each readout, we scale the initial estimate of the count rates by the appropriate fractional exposure time at each readout and subtract them pixel by pixel from each readout. The pixel median of each resulting frame is then an estimate of the "pedestal constant" for that readout and can be subtracted. Finally, the entire slope-fitting and cosmic-ray rejection process is repeated, yielding a sky-subtracted, flat-fielded image for each pointing of the telescope.

Next, each of the four individual target images, which has been constructed from the multiple readouts, is magnified by a factor of 2 using third-order spline interpolation. Then all four are registered, after the dither shifts are determined from a two-dimensional cross-correlation. To construct the combined, final image, they are weighted inversely by the sky variance and co-added. During the image combination, bad pixels are removed using a mask file and the IRAF "avsigclip" 3 σ rejection algorithm. We also produce separate combinations for each exposure where the other exposures have been relative

---

[12] The package may be downloaded from http://cfa-www.harvard.edu/castles.

weights a factor of 1000 smaller. This results in shifted, masked, and clipped images for each subexposure, which we used to estimate measurement errors.

The analysis of NIC1 data (B0218+357 and B1030+074) is similar to that for the NIC2 data. However, the failure to dither the observations and the limited use of the NIC1 observing mode led to significantly poorer results than for the NIC2 data. The lack of dithering, the use of two different exposure sequences, and the limited use of the observing mode made it impossible to construct empirical sky-darks. The lack of dithering made it impossible to remove bad pixels or chip boundaries. The most important problem was the enormous increase in the background noise caused by cosmic-ray persistence (dark current variations) from SAA passages (Najita, Dickinson, & Holfeltz 1998). The background noise in the NIC1 observations was dominated by cosmic-ray persistence rather than the actual sky background.

REFERENCES

Bahcall, J. N., Hartig, G. F., Jannuzi, B. T., Maoz, D., & Schneider, D. P. 1992b, ApJ, 400, L51
Bahcall, J. N., Maoz, D., Schneider, D. P., Yanny, B., & Doxsey, R. 1992a, ApJ, 392, L1
Bar-Kana, R. 1996, ApJ, 468, 17
Bertin, E., & Arnouts, S. 1996, A&AS, 117, 393
Biggs, A. D., Browne, I. W. A., Helbig, P., Koopmans, L. V. E., Wilkinson, P. N., & Perley, R. A. 1999, MNRAS, 304, 349
Blandford, R. D., & Narayan, R. 1992, ARA&A, 30, 311
Brainerd, T. G., Blandford, R. D., & Smail, I. 1996, ApJ, 466, 623
Browne, I. W. A., Patnaik, A. R., Walsh, D., & Wilkinson, P. N. 1993, MNRAS, 263, L32
Bruzual, A., G., & Charlot, S. 1993, ApJ, 405, 538
Carilli, C. L., Menten, K. M., Reid, M. J., Rupen, M., & Claussen, M. 1998, ASP Conf. Proc. 144, Radio Emission from Galactic and Extragalactic Compact Sources, ed. J. A. Zensus, G. B. Taylor, & J. M. Wrobel (San Francisco: ASP), 317
Carilli, C. L., & Rupen, M. P. 1993, ApJ, 412, L59
Claeskens, J. F., Surdej, J., & Remy, M. 1996, A&A, 305, L9
Combes, F., & Wiklind, T. 1997, ApJ, 486, L79
Courbin, F., Lidman, C., Frye, B., Magain, P., Broadhurst, T. J., Pahre, M. A., & Djorgovski, S. G. 1998a, ApJ, 499, L119
Courbin, F., Lidman, C., & Magain, P. 1998b, A&A, 330, 57
Djorgovski, S., & Davis, M. 1987, ApJ, 313, 59
Dressler, A. 1980, ApJ, 236, 351
Dressler, A., Lynden-Bell, D., Burstein, D., Davies, R. L., Faber, S. M., Terlevich, R., & Wegner, G. 1987, ApJ, 313, 42
Fabbiano, G. 1989, ARA&A, 27, 87
Faber, S. M., et al. 1997, AJ, 114, 1771
Falco, E., et al. 1999, ApJ, 523, 617
Fassnacht, C. 1997, BAAS, 191, 5903
Frye, B. L., Courbin, F., Broadhurst, T. J., Welch, W. J. W., Lidman, C., Magain, P., Pahre, M., & Djorgovski, S. G. 1999, in ASP Conf. Proc. 156, Highly Redshifted Radio Lines, ed. C. L. Carilli, S. J. E. Radford, K. M. Menten, & G. I. Langston (San Francisco: ASP), 240
Fukugita, M., & Turner, E. L. 1991, MNRAS, 253, 99
Gerin, M., Phillips, T. G., Benford, D. J., Young, K. H., Menten, K. M., & Frye, B. 1997, ApJ, 488, L31
Grundahl, F., & Hjorth, J. 1995, MNRAS, 275, 67P
Guiderdoni, B., & Rocca-Volmerange, B. 1988, A&AS, 74, 185
Hernquist, L. 1990, ApJ, 356, 359
Hewett, P. C., Irwin, M. J., Foltz, C. B., Harding, M. E., Corrigan, R. T., Webster, R. L., & Dinshaw, N. 1994, AJ, 108, 1534
Holtzman, J., et al. 1995, PASP, 107, 1065
Impey, C. D., Falco, E. E., Kochanek, C. S., Lehár, J., McLeod, B. A., Rix, H.-W., Peng, C. Y., & Keeton, C. R. 1998, ApJ, 509, 551
Jackson, N., Helbig, P., Browne, I., Fassnacht, C. D., Koopmans, L., Marlow, D., & Wilkinson, P. N. 1998, A&A, 334, 33
Jackson, N., Xanthopoulos, E., & Browne, I. W. A. 2000, MNRAS, 311, 389
Jaffe, W. 1983, MNRAS, 202, 995
Jauncey, D. L., et al. 1991, Nature, 352, 132
Jones, D. L., et al. 1993, in Subarcsecond Radio Astronomy, ed. R. J. Davis & R. S. Booth (Cambridge: Cambridge Univ. Press), 150
Keeton, C. R., & Kochanek, C. S. 1996, in IAU Symp. 173, Astrophysical Applications of Gravitational Lensing, ed. C. S. Kochanek & J. N. Hewitt (Dordrecht: Kluwer), 419
———. 1998, ApJ, 495, 157
Keeton, C. R., Kochanek, C. S., & Falco, E. E. 1998, ApJ, 509, 561 (KKF)
Keeton, C. R., Kochanek, C. S., & Seljak, U. 1997, ApJ, 482, 604
Kochanek, C. S. 1993, ApJ, 417, 438
———. 1994, ApJ, 436, 56
———. 1995, ApJ, 445, 559
———. 1996, ApJ, 466, 637
Kochanek, C. S., Falco, E. E., Impey, C. D., Lehár, J., McLeod, B. A., Rix, H.-W., Keeton, C. R., & Peng, C. Y. 2000a, ApJ, in press (astro-ph/9809371)
Kochanek, C. S., Falco, E., Impey, C. D., Lehár, J., Rix, H.-W., Keeton, C. R., Muñoz, J. A., & Peng, C. Y. 2000b, ApJ, submitted (astro-ph/9909018)
Kochanek, C. S., Falco, E. E., Schild, R., Dobrzycki, A., Engels, D., & Hagen, H.-J. 1997, ApJ, 479, 678
Kochanek, C. S., & Narayan, R. 1992, ApJ, 401, 461

Krist, J. E., & Hook, R. N. 1997, The Tiny Tim User's Guide, version 4.4 (Baltimore: STScI)
Kundić, T., et al. 1997, ApJ, 482, 75
Lawrence, C. L. 1996, in IAU Symp. 173, Astrophysical Applications of Gravitational Lensing, ed. C. S. Kochanek & J. N. Hewitt (Dordrecht: Kluwer), 299
Leitherer, C., et al. 1996, PASP, 108, 996
Lidman, C., Meylan, G., Broadhurst, T., Frye, B., & Welch, W. J. W. 1999, ApJ, 514, L57
Lovell, J. E. J., Jauncey, D. L., Reynolds, J. E., Wieringa, M. H., King, E. A., Tzioumis, A. K., McCulloch, P. M., & Edwards, P. G. 1998, ApJ, 508, L51
Lovell, J. E. J., et al. 1996, ApJ, 472, L5
Lubin, L. M., Fassnacht, C. D., Readhead, A., Blandford, R. D., & Kundić, T. 2000, AJ, 119, 451
MacAlpine, G. M., & Feldman, F. R. 1982, ApJ, 261, 412
MacKenty, J. W., et al. 1997, NICMOS Instrument Handbook, Version 2.0 (Baltimore: STScI)
Magain, P., Surdej, J., Vanderriest, C., Pirenne, B., & Hutsemékers, D. 1992, A&A, 253, L13
Maoz, D., et al. 1992, ApJ, 386, L1
Maoz, D., & Rix, H.-W. 1993, ApJ, 416, 425
Mathur, S., & Nair, S. 1997, ApJ, 484, 140
McLeod, B. 1997, in 1997 HST Calibration Workshop, ed. S. Casertano, R. Jedrzejewski, C. D. Keyes, & M. Stevens (Baltimore: STScI), 281
McLeod, K. K., Rieke, G. H., & Storrie-Lombardi, L. J. 1999, ApJ, 511, L67
McMahon, R., Irwin, M., & Hazard, C. 1992, Gemini, 36, 1
Nair, S., Narasimha, D., & Rao, A. P. 1993, ApJ, 407, 46
Najita, J., Dickinson, M., & Holfeltz, S. 1998, Instrument Science Report NICMOS-98-001 (Baltimore: STScI)
Navarro, J. F., Frenk, C. S., & White, S. D. 1996, ApJ, 462, 563
Oscoz, A., Miquel, S.-R., Mediavilla, E., Buitrago, J., & Goicoechea, L. J. 1997, ApJ, 491, L70
Patnaik, A. R., Browne, I. W. A., King, L. J., Muxlow, T. W. B., Walsh, D., & Wilkinson, P. N. 1993, MNRAS, 261, 435
Patnaik, A. R., Porcas, R. W., & Browne, I. W. A. 1995, MNRAS, 274, L5
Persson, S. E., Murphy, D. C., Krzeminski, W., Roth, M., & Rieke, M. J. 1998, AJ, 116, 2475
Press, W. H., Flannery, B. P., Teukolsky, S. A., & Vetterling, W. T. 1988, Numerical Recipes in C (Cambridge: Cambridge Univ. Press)
Remy, M., Claeskens, J.-F., Surdej, J., Hjorth, J., Refsdal, S., Wucknitz, O., Sorensen, A. N., & Gruhdahl, F. 1998, NewA, 3, 379
Rix, H.-W., de Zeeuw, P., Cretton, N., van der Marel, R. P., & Carollo, C. M. 1997, ApJ, 488, 702
Rix, H.-W., Falco, E. E., Impey, C. D., Kochanek, C. S., Lehár, J., McLeod, B. A., Muñoz, J., & Peng, C. Y. 1999, in ASP Conf. Proc., Gravitational Lensing, ed. T. Brainerd & C. Kochanek (San Francisco: ASP), in press (astro-ph/9910190)
Schechter, P., et al. 1997, ApJ, 475, 85
Schild, R., & Thomson D. J. 1995, AJ, 109, 1970
Schneider, D. P., Gunn, J. E., Turner, E. L., Lawrence, C. R., Hewitt, J. N., Schmidt, M., & Burke, B. F. 1986, AJ, 91, 991
Schneider, P., Ehlers, J., & Falco, E. E. 1992, Gravitational Lenses (Berlin: Springer)
Siemiginowska, A., Bechtold, J., Aldcroft, T. L., McLeod, K. K., & Keeton, C. R. 1998, ApJ, 503, L118
Skinner, C. J. 1997, in HST Calibration Workshop with a New Generation of Instruments, ed. S. Casertano, R. Jedrzejewski, T. Keyes, & M. Stevens (Baltimore: STScI), 233
Steidel, C. C. 1990, ApJS, 72, 1
Subrahmanyan, R., Narasimha, D., Rao, A. P., & Swarup, G. 1990, MNRAS, 246, 263
Surdej, J., Claeskens, J.-F., Remy, M., Refsdal, S., Pirenne, B., Prieto, A., & Vanderriest, C. 1997, A&A, 327, L1
Surdej, J., et al. 1987, Nature, 329, 695
Surdej, J., Magain, P., Borgeest, U., Courvoisier, T. J.-L., Kayser, R., Kellerman, K. I., Kuhr, H., & Refsdal, S. 1988, A&A, 198, 49
Surdej, J., Remy, M., Smette, A., Claeskens, J.-F., Magain, P., Refsdal, S., Swings, J.-P., & Verón-Cetty, M. 1994, in Gravitational Lenses in the Universe, ed. J. Surdej, D. Fraipont-Caro, S. Refsdal, & M. Remy (Liège: Univ. Liège), 153
Thompson, D., Djorgovski, S., & Trauger, J. 1995, AJ, 110, 963

Turner, E. L., Ostriker, J. P., & Gott, J. R. 1984, ApJ, 284, 1
van Dokkum, P. G., Franx, M., Kelson, D. D., & Illingworth, G. D. 1998, ApJ, 504, L17
Wiklind, T., & Combes, F. 1995, A&A, 299, 382
———. 1996, Nature, 379, 139

Wisotzki, L., Kohler, T., Ikonomou, M., & Reimers, D. 1995, A&A, 297, L59
Wisotzki, L., Kohler, T., Kayser, R., & Reimers, D. 1993, A&A, 278, L15
Xanthopoulos, E., et al. 1998, MNRAS, 300, 649
Zaritsky, D. 1994, AJ, 108, 1619